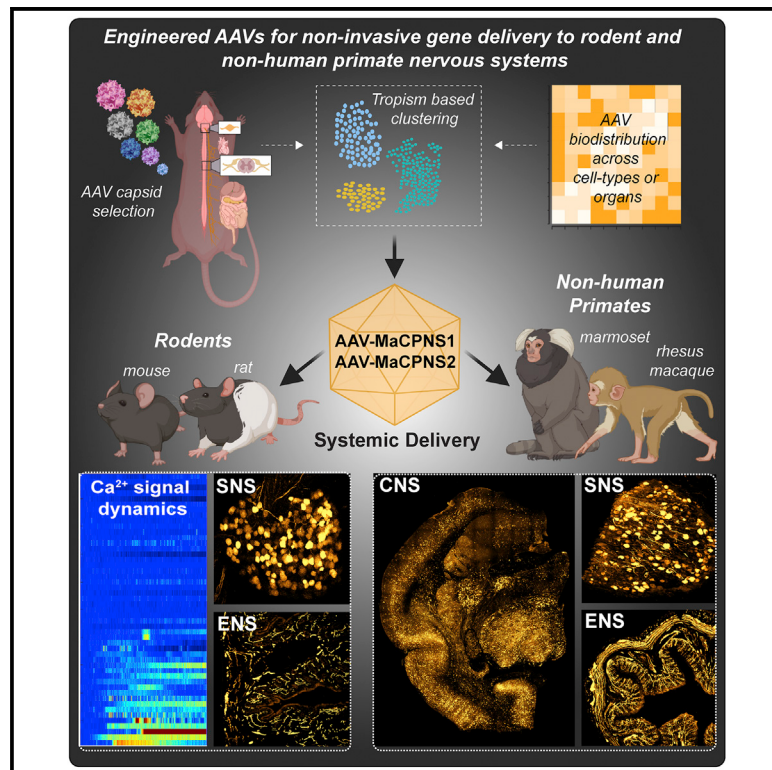


## Engineered AAVs for non-invasive gene delivery to rodent and non-human primate nervous systems

### Graphical abstract



### Authors

Xinhong Chen,  
Sripriya Ravindra Kumar,  
Cameron D. Adams, ..., Andrew S. Fox,  
Isaac M. Chiu, Viviana Gradinaru

### Correspondence

viviana@caltech.edu

### In brief

Chen et al. evolved a family of AAV capsid variants, including MaCPNS1 and MaCPNS2, that efficiently transduced the PNS in rodents following systemic administration, enabling functional readout and non-invasive modulation of PNS. Both vectors could also enable efficient gene delivery to both PNS and CNS in macaque and marmoset.

### Highlights

- Directed evolution in rodents identified AAV vectors targeting the PNS
- Systemically administrated MaCPNS1 and MaCPNS2 efficiently target the PNS in rodents
- Systemic MaCPNS1 is used for functional readout and non-invasive modulation of the PNS
- Systemic MaCPNS1 and MaCPNS2 transduce both the PNS and CNS in macaque and marmoset

## NeuroResource

# Engineered AAVs for non-invasive gene delivery to rodent and non-human primate nervous systems

Xinhong Chen,<sup>1,6</sup> Sripriya Ravindra Kumar,<sup>1,6</sup> Cameron D. Adams,<sup>2</sup> Daping Yang,<sup>3</sup> Tongtong Wang,<sup>1</sup> Damien A. Wolfe,<sup>1</sup> Cynthia M. Arokiaraj,<sup>1</sup> Victoria Ngo,<sup>4</sup> Lillian J. Campos,<sup>5</sup> Jessica A. Griffiths,<sup>1</sup> Takako Ichiki,<sup>1</sup> Sarkis K. Mazmanian,<sup>1</sup> Peregrine B. Osborne,<sup>2</sup> Janet R. Keast,<sup>2</sup> Cory T. Miller,<sup>4</sup> Andrew S. Fox,<sup>5</sup> Isaac M. Chiu,<sup>3</sup> and Viviana Gradinaru<sup>1,7,\*</sup>

<sup>1</sup>Division of Biology and Biological Engineering, California Institute of Technology, Pasadena, CA 91125, USA

<sup>2</sup>Department of Anatomy and Physiology, University of Melbourne, Parkville, Melbourne, VIC 3010, Australia

<sup>3</sup>Department of Immunology, Blavatnik Institute, Harvard Medical School, Boston, MA 02115, USA

<sup>4</sup>Cortical Systems and Behavior Laboratory, University of California, San Diego, La Jolla, CA 92039, USA

<sup>5</sup>Department of Psychology and California National Primate Research Center, University of California, Davis, Davis, CA 95616, USA

<sup>6</sup>These authors contributed equally

<sup>7</sup>Lead contact

\*Correspondence: [viviana@caltech.edu](mailto:viviana@caltech.edu)

<https://doi.org/10.1016/j.neuron.2022.05.003>

## SUMMARY

Gene therapy offers great promise in addressing neuropathologies associated with the central and peripheral nervous systems (CNS and PNS). However, genetic access remains difficult, reflecting the critical need for the development of effective and non-invasive gene delivery vectors across species. To that end, we evolved adeno-associated virus serotype 9 (AAV9) capsid in mice and validated two capsids, AAV-MaCPNS1 and AAV-MaCPNS2, across rodent species (mice and rats) and non-human primate (NHP) species (marmosets and rhesus macaques). Intravenous administration of either AAV efficiently transduced the PNS in rodents and both the PNS and CNS in NHPs. Furthermore, we used AAV-MaCPNS1 in mice to systemically deliver the following: (1) the neuronal sensor jGCaMP8s to record calcium signal dynamics in nodose ganglia and (2) the neuronal actuator DREADD to dorsal root ganglia to mediate pain. This conclusively demonstrates the translatability of these two systemic AAVs across four species and their functional utility through proof-of-concept studies in mice.

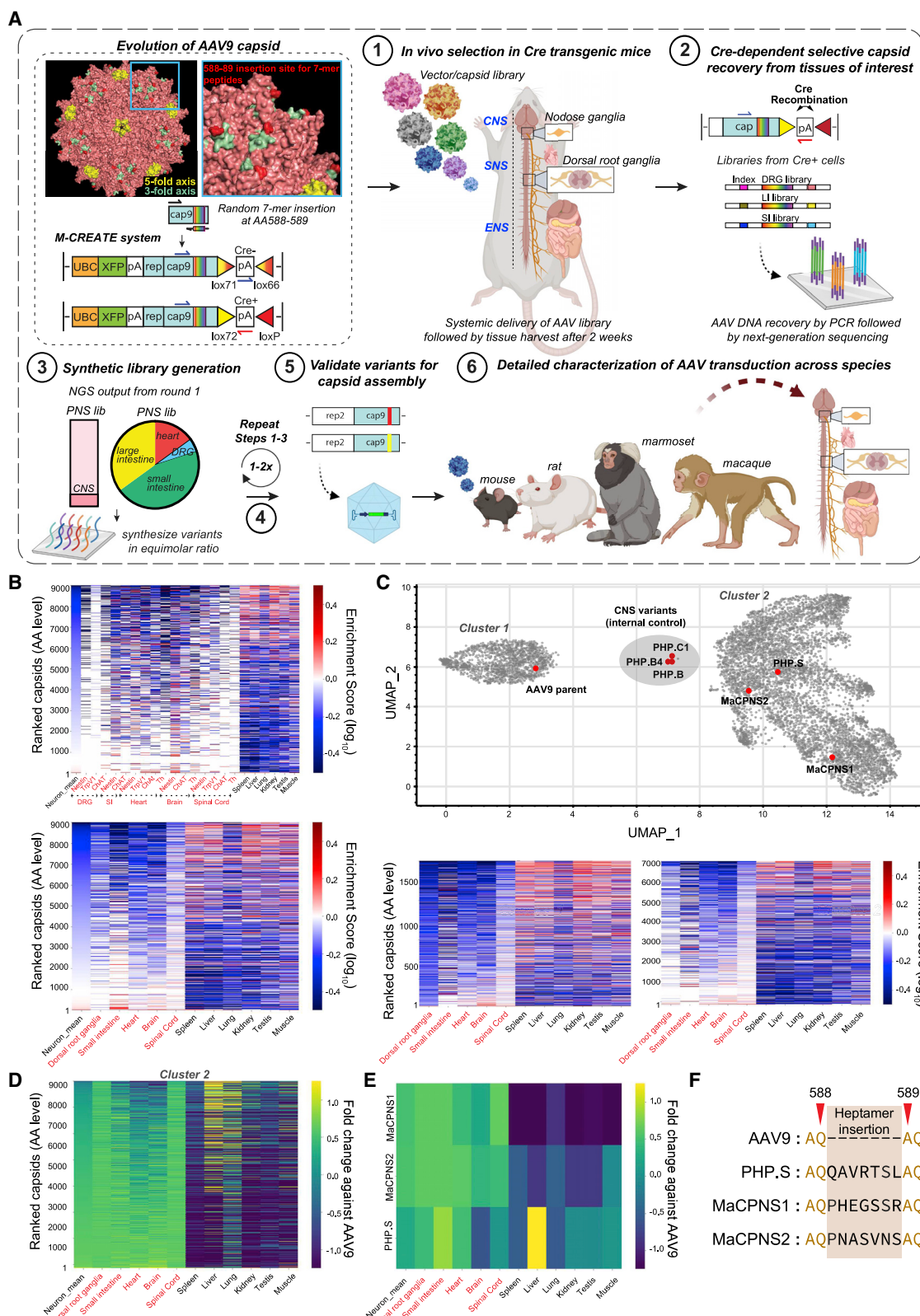
## INTRODUCTION

Gene delivery to the central and peripheral nervous systems (CNS and PNS) has greatly accelerated neuroscience research in the last decade and has the potential to translate this research into novel therapies for neurological disorders. However, the lack of potent vectors enabling non-invasive gene delivery across species is a significant bottleneck that can hinder fast progress ([Ingusci et al., 2019](#); [Pena et al., 2020](#); [Piguet et al., 2021](#)).

The success of gene delivery relies on a safe and efficient vector, and therefore, most *in vivo* applications use adeno-associated viral (AAV) vectors. AAVs offer several advantages, including stable, long-term transgene expression and low immunogenicity ([Bedbrook et al., 2018](#); [O'Carroll et al., 2021](#)). The natural serotypes of AAV have demonstrated considerable success in targeting different cell populations within the nervous system through direct routes of gene delivery, such as intracranial ([Golebiowski et al., 2017](#); [GuhaSarkar et al., 2017](#)), intracerebroventricular (i.c.v.) ([Bey et al., 2020](#)), intrathecal ([Hirai et al., 2012](#)), intraganglionic ([Yu et al., 2013](#)), intrasciatic ([Homs et al., 2011](#)), and intracolonic ([Gore et al., 2019](#)). These direct delivery routes

suffer from limitations, however, including the need for invasive surgery. In addition, anatomical barriers may restrict surgical access (such as for nodose ganglia [NG] or dorsal root ganglia [DRG]). Finally, localized delivery can lead to incomplete coverage of a large complex system such as the enteric nervous system (ENS) or CNS, and multiple direct interventions may be needed to increase coverage ([Gray et al., 2010](#)).

An alternative, non-invasive intravenous (i.v.) route circumvents these limitations. Some natural serotypes, including AAV9, can target the CNS or PNS systemically. However, lack of specificity toward the target and low efficiency, necessitating high vector load, both potentially lead to toxicity ([Bourdenx et al., 2014](#); [Yang et al., 2014](#); [Vogt et al., 2015](#); [Gombash et al., 2017](#)). Years of capsid engineering efforts have now yielded a toolbox of improved CNS capsids for rodents ([Deverman et al., 2016](#); [Körbelin et al., 2016](#); [Ojala et al., 2018](#); [Ravindra Kumar et al., 2020](#); [Nonnenmacher et al., 2021](#)). These include the potent vector AAV-PHP.eB (engineered using CREATE) for the CNS, but its application is restricted to select mice strains ([Deverman et al., 2016](#); [Chan et al., 2017](#); [Hordeaux et al., 2018](#); [Matsuzaki et al., 2018](#); [Hinderer et al., 2018](#)). Unlike PHP.B/eB,



(legend on next page)

the recently engineered AAV-F (engineered using iTransduce) and AAV-PHP.Cs (engineered using Multiplexed-CREATE or M-CREATE) for the CNS work across mouse strains (Hanlon et al., 2019; Ravindra Kumar et al., 2020). However, the heterogeneity of the blood-brain barrier (BBB) depending on the genetic background has posed a significant challenge for developing capsids that have the potential to translate across species (Hordeaux et al., 2019; Huang et al., 2019; Batista et al., 2020). This issue is particularly acute for non-human primates (NHPs), which are commonly used as pre-clinical research models for gene therapy (Kimura and Harashima, 2020; Piguet et al., 2021). With several CNS- and PNS-based therapies in the pipeline, there is, therefore, a high demand for next-generation systemic AAV vectors with potent neurotropic behavior to achieve efficient and safe gene delivery for translational applications (Deverman et al., 2018; Tosolini and Smith, 2018; Hudry and Vandenberghe, 2019; Chen et al., 2021; Huang et al., 2021; Challis et al., 2022).

Building on our success in selecting improved CNS-targeting capsids using M-CREATE (Ravindra Kumar et al., 2020; Goertzen et al., 2022), we decided to test the potential of this method for selecting improved PNS-targeting capsids outperforming the prior engineered variant, AAV-PHP.S, which requires a high dose to exhibit its potent PNS tropism via i.v. delivery (Chan et al., 2017). Compared with the CNS, the PNS is a more challenging AAV engineering target. Cell populations are sparser, and there is no strong source of selection pressure across targets (akin to the BBB for the CNS). M-CREATE is uniquely well suited to this problem as it capitalizes on deep recovery of capsid libraries across cell types/organs to select capsids enriched in areas of interest and a customized analysis pipeline that incorporates positive and negative selections to help identify variants with desired properties.

In this study, we used M-CREATE to identify a family of 7-mer containing AAV9 capsids that appeared to be biased toward PNS areas and detailed the properties of two such selected AAVs, AAV-MaCPNS1 and AAV-MaCPNS2, in rodents and NHPs. We provide *in vivo* validation of their tropism in mice and demonstrate their potential applications with proof-of-concept studies for functional readout and modulation of sensory ganglia. In addition

to finding improved PNS-targeting capsids, we sought to address the fundamental question of the translatability of capsids selected in mouse models. To this end, we examined these capsids across the following four species commonly used in basic through pre-clinical applications: mice, rats, marmosets, and rhesus macaques. The variants discussed in this study show improved efficiency and specificity toward the PNS and translate their potent behavior across mammalian species. Interestingly, and potentially due to the heterogeneity of the BBB, these variants also show the efficient crossing of the BBB to infect the CNS in NHPs (Table S1).

## RESULTS

### AAV capsid selection in mice identifies two AAV variants with PNS specificity

As a starting point for capsid engineering, we chose AAV9 due to its broad tropism when delivered systemically, including for the nervous system (both CNS and PNS) (Foust et al., 2009; Bevan et al., 2011). We diversified the AAV9 capsid by inserting a randomized 7-mer peptide between positions 588 and 589 (Figure 1A) and i.v. injected the resulting virus library into adult mice of the following three Cre-transgenic lines: SNAP-Cre (for neurons), GFAP-Cre (for glia), and Tek-Cre (for endothelial cells forming the blood-organ barrier). Two weeks post injection, we processed peripheral tissues (such as the heart, small and large intestines, and DRG) and selectively extracted viral genomes from Cre+ cells using Cre-dependent PCR (see STAR Methods; Figure 1A2).

After round-1 (R1) selection, we recovered a total of ~9,000 variants from the Cre lines in the following PNS tissues of interest: the heart, DRG, and small and large intestine. Of these, ~10% overlapped with the CNS libraries (Figure 1A3). We then synthesized these variants in an equimolar ratio to create a synthetic oligopool library for round-2 (R2) PNS selection. This synthetic pool also included a spike-in library of previously validated internal controls (see STAR Methods). We i.v. injected the R2 virus library into different Cre lines as follows: Nestin-Cre (for neurons), CHAT-Cre (for cholinergic neurons), TRPV1-Cre (for primary afferent thermosensitive neurons), and Tek-Cre (for

**Figure 1. Multiplexed-CREATE selection for AAV capsids targeting the nervous system across species**

- (A) An overview of the capsid selection method, Multiplexed-CREATE, and characterization of selected capsids across species. The top left panel illustrates the evolution of the AAV9 capsid (PDB 3UX1) with a zoom-in (blue) of a 3-fold axis and the 7-mer-i library insertion site between residues 588–589 highlighted in red. The diagrams below demonstrate the arrangement of the acceptor vector in the absence (top) or presence (bottom) of Cre, with the corresponding orientations of the forward/reverse primers used for Cre+ selective recovery. The selection workflow involves four key steps: (1) generation of capsid library and intravenous (i.v.) delivery into transgenic mouse lines where Cre is restricted to cell types of interest (SNAP-Cre, GFAP-Cre, Tek-Cre, n = 2 mice per Cre line). (2) Two weeks post injection, viral DNA is recovered across cell types/tissues using Cre-dependent PCR and Illumina next-generation sequencing (NGS) and (3) fed into synthetic pool library production. (4) This library then goes through a second round of *in vivo* selection. Following this selection process, identified variants are validated for (5) virus production and (6) *in vivo* transduction across species.
- (B) Heatmaps of capsid variants' mean enrichment by Cre-dependent recovery across tissues of interest (red text) and Cre-independent recovery across off-targets (black text) after two rounds of selection. Cre lines are plotted separately (top panel, n = 3 mice per organ) or grouped by organs (bottom panel). The y axis represents capsids unique at the amino acid (aa) level, ranked by "neuron mean," which is the mean of the enrichment of all targets of interest.
- (C) UMAP cluster representation of ~9,000 variants that were recovered after two rounds of selection (UMAP parameters: n\_neighbors = 15, min\_dist = 0.1, n\_components = 2, random\_state = 42, metric = "correlation," and verbose = 3). Three separable clusters are shown along with the positions of known capsids (AAV9, PHP.S, PHP.B, PHP.B4, and PHP.C1) and new capsids (MaCPNS1 and MaCPNS2). Heatmaps (below) show enrichment of representative capsids from clusters-1 and -2 across organs.
- (D) Heatmap of enrichment fold changes against parental AAV9 across organs.
- (E) Heatmap of enrichment fold changes against parental AAV9 of variants MaCPNS1 and MaCPNS2 and previously engineered variant PHP.S across organs.
- (F) Identity of hepta-AA peptides inserted between positions 588–589 of AAV9 for PHP.S, MaCPNS1, and MaCPNS2 capsids.

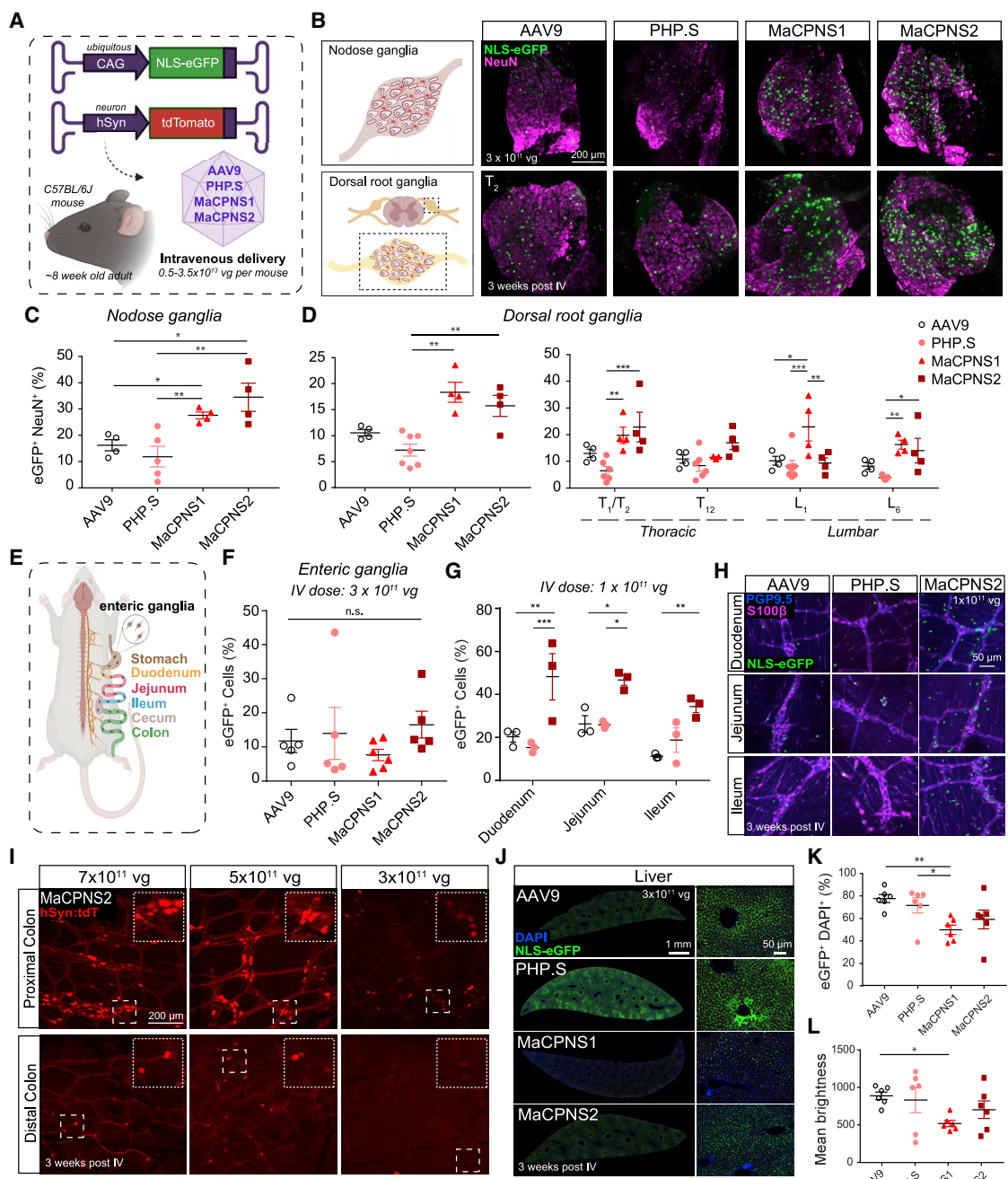


**Figure 2. Engineered AAVs can efficiently target the peripheral nervous system in mice following systemic delivery**

(A) Illustration demonstrating the i.v. administration of AAV capsids packaged with ssAAV:CAG-2xNLS-eGFP and ssAAV:hSyn-tdTomato genome in a mouse model (~8-week-old young C57BL/6J adults).

(B) (Top) An illustration of the nodose ganglia (NG) (left), and the representative images of AAV9, PHP.S, MaCPNS1, and MaCPNS2 vector-mediated expression of nuclear-localized (NLS) eGFP (green) in NG (right). (Bottom) An illustration of the dorsal root ganglia (DRG) in the spinal cord (left) and (right) representative images of AAV vector-mediated expression of NLS-eGFP (green) in DRG across segment T2 (thoracic) of the spinal cord ( $n \geq 4$  per group, ~8-week-old C57BL/6J males,  $3 \times 10^{11}$  vg i.v. dose per mouse, and 3 weeks of expression). Magenta:  $\alpha$ NeuN antibody staining for neurons. Images are matched in fluorescence intensity to the respective AAV9 control. Scale bar, 200  $\mu$ m.

(C) Percentage of AAV-mediated eGFP expression overlapping with the  $\alpha$ NeuN marker in NG. One-way ANOVA non-parametric Kruskal-Wallis test (exact  $p = 0.0003$ ), and follow-up multiple comparisons with uncorrected Dunn's test are reported ( $p = 0.0499$  for AAV9 versus MaCPNS1,  $p = 0.0251$  for AAV9 versus MaCPNS2,  $p = 0.0094$  for PHP.S versus MaCPNS1, and  $p = 0.0038$  for PHP.S versus MaCPNS2). \* $p \leq 0.05$  and \*\* $p \leq 0.01$  are shown;  $p > 0.05$  is not shown;  $n \geq 4$  per group, same experimental parameters as (B). Each data point represents 1–2 nodose ganglia per mouse comprising >700 cells, mean  $\pm$  SEM is plotted.

(legend continued on next page)

endothelial cells, providing negative selection). Two weeks post injection, we selectively recovered capsids by Cre-dependent PCR from tissues of interest (the DRG, heart, small and large intestine, brain, and spinal cord [SC]) and other targets (the spleen, liver, lung, kidney, testis, and muscle) by performing a Cre-independent PCR (see **STAR Methods**; **Figures 1A4** and **1B**).

After two rounds of *in vivo* selection, among all the variants that we included in the R2 library, 6,300 variants showed a bias toward one or more of the PNS tissues (**Figures 1B** and **S1A**). We next sought to further classify the recovered variants based on distinct tropisms. We used the uniform manifold approximation and projection (UMAP) algorithm (McInnes et al., 2020), which takes into account differences among variants' enrichments across organs, to identify clusters of variants representing distinct tropisms (**Figure 1C**, top panel). Members of cluster-1 (1,846 variants), which includes AAV9, showed relatively higher enrichment in off-target tissues such as the liver (**Figure 1C**, bottom left panel). Cluster-2 members (7,148 variants), including our previously engineered variant PHP.S, exhibited relatively higher enrichment in the PNS and lower enrichment in off-target tissues (**Figure 1C**, bottom right panel). Cluster-3 members (5 variants), including variants from the internal control, were highly enriched in the CNS.

Based on this analysis, we reasoned that cluster-2 might contain promising variants distinct from the parental AAV9, which we indeed observed by comparing their tropism directly to that of AAV9 (**Figure 1D**). We identified two new capsids from cluster-2

that exhibited low off-target transduction compared with AAV9 and PHP.S (**Figure 1E**) and that could package viral genomes with similar efficiency to AAV9 (see **STAR Methods**; **Figure S1B**). We will henceforth refer to the first capsid, with a 7-mer peptide insertion of PHEGSSR between the 588–89 residues of the AAV9 parent, as AAV-MaCPNS1 and the second, with an insertion of PNASVNS, as AAV-MaCPNS2 (**Figure 1F**).

#### IV-delivered AAV-MaCPNS1/2 efficiently transduces sensory and enteric ganglia in mice with low liver transduction

To characterize the transduction capability of AAV-MaCPNS1 and AAV-MaCPNS2 variants *in vivo*, we packaged these variants with a single-stranded (ss) AAV genome carrying a strong ubiquitous promoter, CAG, driving expression of nuclear-localized eGFP reporter and i.v. injected them into adult mice at  $3 \times 10^{11}$  vg per animal (**Figures 2A–2H** and **2J–2L**; see **STAR Methods**). By quantifying expression in NG that overlapped with the NeuN neuronal marker, we found that MaCPNS1 and MaCPNS2 had mean transduction efficiencies of ~28% and ~35%, respectively. By comparison, the efficiency of AAV9 was ~16% and AAV-PHP.S ~12% (**Figures 2B** and **2C**). Thus, MaCPNS1/2 capsids exhibit about 2-fold higher transduction of NG than previously available vectors.

Next, we investigated the efficiency of DRG transduction from selected spinal levels (thoracic and lumbar). The MaCPNS1 vector demonstrated a mean transduction efficiency of ~18% and MaCPNS2 ~16%, compared with ~11% for AAV9 and ~7%

(D) Percentage of eGFP expression overlapping with the  $\alpha$ NeuN marker in the DRG (left) where each data point shows the mean per mouse across select DRGs within thoracic and lumbar segments of the spinal cord. A one-way ANOVA, non-parametric Kruskal-Wallis test (exact  $p = 0.0005$ ), and follow-up multiple comparisons with uncorrected Dunn's test are reported ( $p = 0.0018$  for PHP.S versus MaCPNS1 and  $p = 0.0087$  for PHP.S versus MaCPNS2). \* $p \leq 0.05$  and \*\* $p \leq 0.01$  are shown,  $p > 0.05$  is not shown;  $n \geq 4$  per group, same experimental parameters as (B). Each data point shows the mean  $\pm$  SEM of DRGs across different areas of each mouse, comprising a mean of 1–2 DRGs per area with  $>200$   $\alpha$ NeuN+ cells per DRG. (Right) Percentage of eGFP expression overlapping with the  $\alpha$ NeuN marker in DRG across spinal cord areas in individual mice. A two-way ANOVA and Tukey's multiple comparisons tests with adjusted  $p$  values are reported (\* $p \leq 0.05$ , \*\* $p \leq 0.01$ , and \*\*\* $p \leq 0.001$  are shown; and  $p > 0.05$  is not shown). Each data point shows the mean  $\pm$  SEM of 1–2 DRG per mouse comprising  $>200$   $\alpha$ NeuN+ cells per DRG.

(E) Illustration of the adult mouse gastrointestinal (GI) tract, highlighting the enteric ganglia (zoom-in) that are spread across the different segments of the GI tract. (F) Percentage of cells expressing NLS-eGFP delivered by AAV vectors in the myenteric plexus across the GI tract: stomach, duodenum, jejunum, ileum, proximal colon, and cecum (ssAAV:CAG-2xNLS-eGFP genome,  $n \geq 5$  per group,  $\sim 8$  weeks old C57BL/6J males,  $3 \times 10^{11}$  vg i.v. dose per mouse, and 3 weeks of expression). A one-way ANOVA non-parametric Kruskal-Wallis test (approximate  $p = 0.2985$ ), and follow-up multiple comparisons using uncorrected Dunn's test are reported (individual  $p > 0.05$ , n.s.). Each data point shows the mean  $\pm$  SEM of  $>100$  enteric ganglia per intestinal segment per mouse.

(G) Percentage of cells expressing NLS-eGFP (green in H) in the myenteric plexus of small intestinal segments: duodenum, jejunum, and ileum delivered by AAV vectors: AAV9, PHP.S, and MaCPNS2 (ssAAV:CAG-2xNLS-eGFP genome,  $n = 3$  per group,  $1 \times 10^{11}$  vg i.v. dose per mouse, and 3 weeks of expression). Two-way ANOVA, Tukey's multiple comparisons tests with adjusted  $p$  values are reported (\* $p \leq 0.05$ , \*\* $p \leq 0.01$ , and \*\*\* $p \leq 0.001$  are shown;  $p > 0.05$  is not shown). Each data point shows the mean  $\pm$  SEM of  $\geq 2$  images per mouse comprising  $>100$  enteric ganglia.

(H) Shows representative images of AAV-mediated eGFP expression across the individual intestinal segments analyzed in (G). Scale bar, 50  $\mu$ m. The tissues were co-stained with  $\alpha$ S100 $\beta$  (magenta) antibodies for glia and  $\alpha$ PGP9.5 (blue) for neurons. The images are matched in fluorescence intensity to the respective AAV9 control.

(I) MaCPNS2 vector-mediated expression of tdTomato (red) from ssAAV:hSyn-tdTomato in the proximal and distal segments of the colon at three different i.v. doses per mouse:  $7 \times 10^{11}$  vg,  $5 \times 10^{11}$  vg, and  $3 \times 10^{11}$  vg (3 weeks of expression;  $n = 3$  per group; scale bar, 200  $\mu$ m; and the dotted white box inset represents a zoomed-in view of the indicated area in each image). Images in the distal and proximal colon are matched in fluorescence intensity.

(J) Representative images of AAV vector-mediated expression of NLS-eGFP (green) from ssAAV:CAG-2xNLS-eGFP in the liver ( $n = 6$  per group;  $3 \times 10^{11}$  vg i.v. dose/mouse; and 3 weeks of expression; blue: DAPI staining of nuclei; scale bar, 1 mm [left, full cross-sectional image], and 50  $\mu$ m [right, higher magnification view]). The images are matched in fluorescence intensity to the respective AAV9 control.

(K) Percentage of eGFP+ cells overlapping with the DAPI marker in the liver. A non-parametric Kruskal-Wallis test (approximate  $p = 0.0168$ ), and follow-up multiple comparisons with uncorrected Dunn's test ( $p = 0.0035$  for AAV9 versus MaCPNS1 and  $p = 0.0189$  for PHP.S versus MaCPNS1) are reported (\* $p \leq 0.05$  and \*\* $p \leq 0.01$  are shown;  $p > 0.05$  is not shown; same experimental parameters as J; each data point shows the mean  $\pm$  SEM of 4 images per mouse comprising  $>780$  DAPI+ cells per image).

(L) Mean brightness of the eGFP+ cells quantified in K. A non-parametric Kruskal-Wallis test (approximate  $p = 0.1698$ ) and follow-up multiple comparisons with uncorrected Dunn's test ( $p = 0.0433$  for AAV9 versus MaCPNS1) are reported (\* $p \leq 0.05$  is shown and  $p > 0.05$  is not shown; each data point shows the mean  $\pm$  SEM of 4 images per mouse comprising  $>780$  DAPI+ cells per image).

for AAV-PHP.S (**Figure 2B**, bottom panel; **Figure 2D**, left), with some variability in transduction across different segments of the SC (**Figure 2D**, right). Thus, compared with known capsids, MaCPNS1/2 can achieve about 2-fold higher transduction of DRG via i.v. delivery. Increasing the vector dose to  $1 \times 10^{12}$  vg, we observed that PHP.S had higher transduction in DRG compared with AAV9 whereas MaCPNS1 exhibited even higher transduction (**Figures S2A–S2C**), further confirming that MaCPNS1/2 capsids transduce DRG in adult mice more efficiently than either AAV9 or PHP.S.

To investigate the transduction efficiency of the new vectors in the ENS, we assessed AAV-mediated eGFP expression in the enteric ganglia of the myenteric plexus across different areas of the GI tract—the stomach, duodenum, jejunum, ileum, proximal colon, and cecum (**Figures 2E** and **2F**). We observed a mean transduction efficiency of ~8% by MaCPNS1, ~17% by MaCPNS2, ~13% by PHP.S, and ~12% by AAV9 (**Figure 2F**). By analyzing individual GI segments, we noticed variability in the transduction of enteric ganglia, with a bias of MaCPNS2 transduction toward small intestinal (SI) segments (duodenum, jejunum, and ileum) over other areas, indicating a modest improvement in SI ENS transduction by MaCPNS2 compared with other vectors. To more closely examine this SI bias, we slightly lowered the vector dose to  $1 \times 10^{11}$  vg and observed a 2-fold increase in the transduction of the SI by MaCPNS2 compared with AAV9 (**Figures 2G** and **2H**). Next, we investigated if the transduction efficiency across large intestinal (LI) segments could be improved by a higher dose (**Figures 2I** and **S2D**). Compared with the initial dose of  $3 \times 10^{11}$  vg, we observed that a MaCPNS2 dose of either  $5 \times 10^{11}$  vg or  $7 \times 10^{11}$  vg achieved robust and uniform transduction of the enteric ganglia of the myenteric plexus in the proximal colon as well as sparser transduction in the distal colon. Thus, i.v. administered MaCPNS2 offers improved transduction of enteric ganglia in the SI, with the option of additional targeting of LI segments at higher doses.

To investigate the liver transduction of MaCPNS1/2 capsids, we assessed eGFP expression *in vivo* (**Figures 2J–2L**). MaCPNS1 exhibited 1.5-fold lower transduction compared with the same dose of AAV9 or PHP.S (**Figure 2K**). Quantifying the mean brightness of the eGFP fluorescence signal revealed that the new vectors also exhibited a 1.3- to 2.1-fold lower signal compared with AAV9 or PHP.S (**Figure 2L**), suggesting reduced transgene expression per cell. Collectively, these data suggest that MaCPNS1 exhibits lower transduction of hepatocytes and lower transgene expression per liver cell compared with other vectors used for PNS. In addition to the liver, we also investigated other tissues, including the CNS, given AAV9's ability to cross the BBB. At a modest i.v. dose of  $3 \times 10^{11}$  vg, CNS transduction was low for all vectors we tested, including AAV9 (**Figure S2E**). Even when we increased the dose of MaCPNS2 to  $5\text{--}7 \times 10^{11}$  vg, we did not observe CNS transduction in mice (**Figure S2F**). In addition, MaCPNS1/2 transduction of cardiac muscle was similar to that of AAV9 (**Figure S2E**).

All of the above experiments were conducted in adult mice. However, many potential applications require early age intervention (Gray, 2016; Privilizzi et al., 2021; Ali et al., 2021). Therefore, we investigated MaCPNS1/2 transduction in DRG in neonates using an alternative delivery route. We introduced MaCPNS1/2

capsids packaged with ssAAV:hSyn-tdTomato into postnatal stage 1 (P1) mice via an intraperitoneal (i.p.) injection, with a dose of  $3 \times 10^{11}$  vg per mouse. After 6 weeks of expression, MaCPNS1 transduced ~39% of neurons (marked with Tuj1) in DRG, and MaCPNS2 transduced ~35%, including ~55% of all CGRP+ neurons and ~19% of all NF200+ neurons (**Figures S2G–S2I**). Examining targeting preference, we found that the capsids were predominantly targeting two types of neurons: about 60% of transduced neurons were CGRP+ and ~11% NF200+ (**Figure S2J**).

In summary, we found that systemic delivery of MaCPNS1 and MaCPNS2 vectors in mice can efficiently transduce sensory ganglia (such as NG and DRG) compared with AAV9, with MaCPNS2 distinguished from MaCPNS1 by enhanced transduction of the ENS. Furthermore, MaCPNS1 and MaCPNS2 exhibited improved specificity for the PNS, with relatively lower transduction of AAV9's primary target, the liver.

### Systemic MaCPNS1-mediated sensor and actuator expressions enable functional characterization of neurons in nodose ganglia and dorsal root ganglia

Functional readout of PNS activity during physiological conditions is key to understanding the interaction between the brain and peripheral system (Chen et al., 2017; Zanos et al., 2018; Walters et al., 2019; Jiman et al., 2020). However, commonly used imaging with genetically encoded calcium indicators (GECIs) in the CNS has been challenging in the PNS due to the low efficiency of delivering GECI to PNS targets. To test the applicability of MaCPNS1/2 capsids to this problem, we delivered i.v. MaCPNS1 capsid packaged with a recently developed GECI, jGCaMP8s (Zhang et al., 2020), to adult mice. After three weeks of expression, we recorded calcium signals *in vivo* during procedures on the gut (**Figures 3A–3C**). We infused the gut with either glucose solution or saline (to induce distension) while recording neuronal activity in the NG of the anesthetized mice and observed distinguishable neuronal responses in the NG (**Figures 3A–3C**). No significant expression was observed in the CNS or liver of these mice.

After verifying the new vectors' potential for enabling functional readout of the PNS, we took the further step of seeing whether we could achieve functional modulation with the vectors. We sought to construct a mouse pain-induction system with improved temporal control, a critical tool for understanding and potentially managing pain. To activate DRG TRPV1 neurons, we packaged Cre-dependent excitatory designer receptors exclusively activated by designer drugs (DREADD) (Krashes et al., 2011) into MaCPNS1 and i.p. injected the vector into P1 TRPV1-Cre pups (**Figure 3D**). After 6 weeks of expression (**Figure 3E**), we gave mice an intraplantar injection of the DREADD agonist clozapine N-oxide (CNO) and evaluated the resulting pain-like behaviors (see **STAR Methods**). We observed an increase in the number of bouts and overall time spent lifting or licking the injected footpad in the experimental AAV-administered group compared with the control group, indicating nocifensive pain-like behavior (**Figures 3F** and **3G**).

Together, these results provide a proof of concept for the application of these new vectors to a wide range of studies involving the monitoring and modulation of sensory processes, including pain.

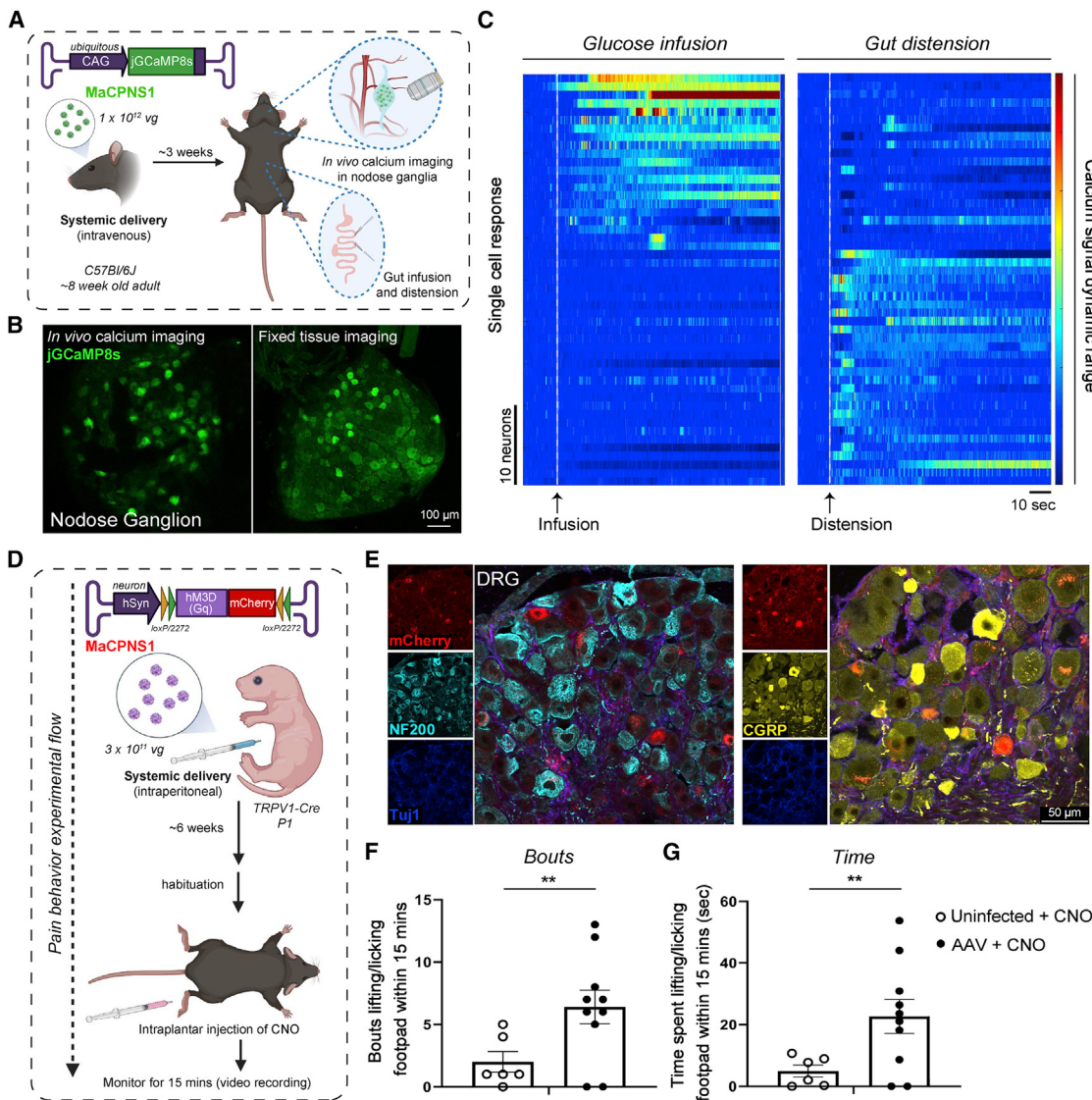


**Figure 3. Systemic delivery of GCaMP sensor and excitatory DREADD actuator using AAV-MaCPNS1 enables functional characterization of DRG neurons in mouse models**

(A) Illustration of i.v. administration of MaCPNS1 capsid packaged with ssAAV:CAG-jGCaMP8s genome in mice (~8-week-old young adults, C57BL/6J males,  $1 \times 10^{12}$  vg i.v. dose/mouse, n = 4). Three weeks post expression, the mice were anesthetized and subjected to *in vivo* calcium imaging in nodose ganglia (NG, top zoom-in) and glucose infusion and distension in the gut (bottom zoom-in).

(B) Representative images of MaCPNS1 vector-mediated expression of jGCaMP8s (green) in NG *in vivo* (left) and in post-hoc fixed tissue (right) (scale bar, 100 μm).

(C) Single-cell activity response measured by calcium signal dynamics in the NG (data pooled from 4 experimental mice). Left panel: NG neuronal response to glucose infusion (white dotted line). Right panel: NG neuronal response to gut distension (white dotted line). Calcium signal dynamic range.

(D) Illustration of the pain induction experimental workflow. MaCPNS1 vector with ssAAV:hSyn-DIO-hM3D(Gq)-mCherry was intraperitoneally administered to a TRPV1-Cre mouse model (postnatal stage 1 [P1], males, and  $3 \times 10^{11}$  vg i.v. dose/mouse). After six weeks of expression, the mice (AAV injected or untreated) were habituated and subjected to intraplantar injection with the agonist CNO after which the mice were monitored for nociceptive lifting/licking behaviors.

(E) Representative images of DRG sections showing MaCPNS1 vector-mediated mCherry (red) expression. The tissues were co-stained with αNF200 (cyan), αTuj1 (blue), and αCGRP (yellow) markers (scale bar, 50 μm).

(F) Total bouts of lifting/licking the footpad within 15 min of injection in uninfected (n = 6) and MaCPNS1-infected (n = 10) mice treated with CNO. \*\*p < 0.01 by unpaired t test. Mean ± SEM is shown.

#### IV-administered AAV-MaCPNS1/2 efficiently transduces the PNS in adult rats

Having validated the new variants' transduction profiles in mouse models, we next investigated their efficacy in another

common research model system—rats. Systemic delivery of MaCPNS1/2 capsids packaged with ssAAV:hSyn-tdTomato in Sprague Dawley adults (Figure 1A) transduced sensory ganglia (DRG and trigeminal ganglia [TG]), sympathetic ganglia

(sympathetic chain ganglia [SCG] and inferior mesenteric ganglia [IMG]), mixed sympathetic-parasympathetic ganglia (the major pelvic ganglion [MPG]), and enteric ganglia across the SI and LI ([Figures 4A–4F](#), [S3A](#), and [S3B](#)). The majority of cells transduced in both DRG and TG were NF200+ (about 70%–75%), with only 5% either CGRP+ or TRPV1+ ([Figures 4C](#) and [4D](#)). In terms of efficiency, both capsids transduced ~22% of the NF200+ cells in DRG and 15%–17% of the NF200+ cells in TG ([Figure 4E](#)). Interestingly, this cell type bias contrasts with what we observed in neonatal mice, where the vectors showed a bias toward CGRP+ neurons ([Figures S2I](#) and [S2J](#)). This profile could result from differences in species or age/time of injection as well as the different systemic routes of vector delivery (similar tropism shifts have been reported elsewhere [[Foust et al., 2009](#)]). The tropism diversity highlights the necessity of considering all relevant experimental variables to achieve the desired transduction profile.

The vectors' efficient labeling of sensory ganglia prompted us to look further into the ENS ([Figures 4F](#) and [S3C](#)). Analyzing segments of the SI and LI, we found that MaCPNS1 and MaCPNS2 were comparable at transducing the myenteric plexus and the submucosal plexus, including the vascular and periglandular plexuses. Next, we investigated projections to the SC and brainstem ([Figures 4G](#) and [S3D](#)). Sensory nerve fibers entering the dorsal horn of the SC were densely labeled, and the ascending afferent tracts in the dorsal column were also strongly transduced by both virus vectors. In the brainstem, fibers were densely labeled in the spinal trigeminal nucleus oralis (Sp5O), which potentially projected from the TG. In addition to the transduction in the PNS and the nerve projections labeling in the CNS, we also observed some labeling of neuronal cell bodies across regions in the brain ([Figure S3D](#)). Furthermore, we observed no expression in the liver ([Figure S3E](#)).

Together, these results show that the potent PNS tropism of the MaCPNS1/2 vectors is conserved across rodent models tested.

#### **IV-delivered AAV-MaCPNS1/2 transduces the adult marmoset CNS and PNS more efficiently than AAV9**

Novel capsids selected in mice do not always translate to NHPs ([Hordeaux et al., 2018](#); [Matsuzaki et al., 2018](#)). After validating the MaCPNS1/2 capsids in mice and rats, we therefore decided to assess their performance in NHPs. First, we chose the marmoset, a New World monkey, and an emerging animal model for translational research. Owing to the limited availability of these animals, in each adult animal we tested two viral capsids (AAV9, MaCPNS1, or MaCPNS2) packaging different fluorescent reporters (either ssAAV:CAG-eGFP or ssAAV:CAG-tdTomato) ([Figure 5A](#)). Compared with the parent AAV9, i.v. delivered MaCPNS1/2 capsids carrying either ssAAV:CAG-eGFP or ssAAV:CAG-tdTomato genome showed robust transduction of the PNS and the CNS. In the PNS, we observed enhanced transduction of DRG, the SI, and the ascending fiber tracts in the dorsal column of the SC ([Figures 5B–5D](#)), similar to what we observed in rodents. In the CNS, robust brain-wide transduction by MaCPNS1/2 capsids, but not AAV9, was evident in regions including the cortex, thalamus, globus pallidus, cerebellum, and brainstem ([Figures 5E](#) and [5F](#)). Further antibody staining

and quantification revealed that capsids mainly transduce neurons and astrocytes in the marmoset brain. In the marmoset cortex, MaCPNS2 displayed a ~5.5-fold increase in neuronal transduction over AAV9 while MaCPNS1 displayed a ~4-fold increase over AAV9 ([Figures S4A–S4C](#)). Among the neurons transduced, few overlapped with the PV marker, indicating the vectors' potential bias to the excitatory population ([Figure S4D](#)). For astrocyte transduction, MaCPNS2 displayed a ~25-fold increase over AAV9 in the cortex ([Figure S4B](#)). Similar improvement in both neuronal and astrocytic transduction was also observed in the thalamus ([Figure S4C](#)).

These results demonstrate that the MaCPNS1/2 capsids can efficiently cross the BBB in adult marmosets while still exhibiting the enhanced PNS tropism observed in rodents.

#### **IV-delivered AAV-MaCPNS1/2 transduces the infant rhesus macaque CNS and PNS more efficiently than AAV9**

Encouraged by the tropism of MaCPNS1/2 capsids in marmosets, we further assessed their transduction potential in another NHP, the rhesus macaque, an Old World monkey, and a common pre-clinical research model for AAV gene therapy. We employed the same strategy as in marmosets, i.v. administering AAV9, MaCPNS1, and MaCPNS2 capsids packaging either ssAAV:CAG-eGFP or ssAAV:CAG-tdTomato to an infant rhesus macaque ([Figure 6A](#)). Similar to our results in marmosets, we observed that MaCPNS1/2 efficiently targeted both the CNS and PNS compared with the parent AAV9 after three weeks of expression. We saw enhanced transduction in the SC, DRG, and GI tract, including the esophagus, colon, and SI ([Figures 6B–6D](#)), as observed in rodents and marmosets. In the SC, there was strong labeling of both ascending fiber tracts in the dorsal column as well as the peripheral fiber tracks coming into the dorsal horn. Within the gray matter of the lumbar SC, MaCPNS1 displayed a ~25-fold increase in neuronal transduction over AAV9. For non-neuronal cells, MaCPNS2 displayed a ~130-fold increase in transduction over AAV9 ([Figures S5A](#) and [S5B](#)). Similar improvement in transduction was also observed in the thoracic SC ([Figures S5C](#) and [S5D](#)). In the lumbar and thoracic DRG, MaCPNS2 displayed ~77-fold and ~44-fold increases in neuronal transduction over AAV9, respectively. MaCPNS1 also showed ~37-fold and ~22-fold increases in neuronal targeting in lumbar and thoracic DRG. Within lumbar DRG ([Figure S5E](#)), MaCPNS2 was highly specific to neurons, with ~94% of all transduced cells being neurons. In thoracic DRG, both vectors displayed high specificity in targeting neurons ([Figure S5F](#)). In the CNS, MaCPNS1/2 capsids mediated enhanced brain-wide transduction, including in areas such as the cortex, hippocampus, putamen, and brainstem ([Figures 6E](#), [6F](#), and [S6](#); [Videos S1–S4](#)), similar to our observations in marmosets. Both vectors transduced neurons and astrocytes but not oligodendrocytes or endothelial cells ([Figures S7A](#) and [S7B](#)). In the macaque cortex, neuron transduction by MaCPNS1 and MaCPNS2 was ~6-fold and ~11-fold higher, respectively, than AAV9 ([Figure S7B](#)). Most neurons transduced by both vectors were PV-, indicating a potential bias to excitatory populations ([Figure S7D](#)). MaCPNS2 also displayed a ~44-fold increase in astrocyte transduction over AAV9 in the cortex ([Figure S7B](#)).

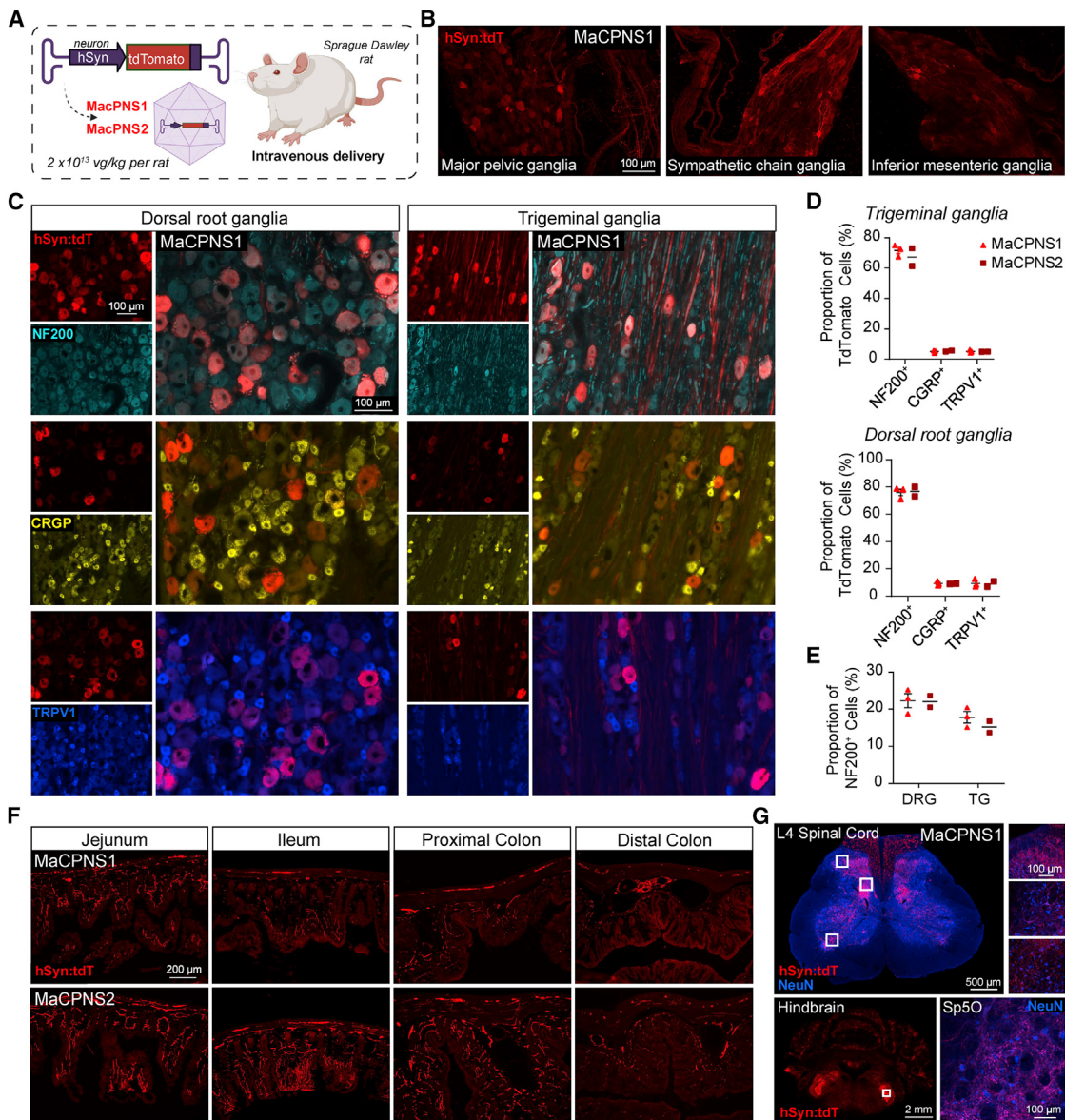


**Figure 4. Engineered AAVs can efficiently target the peripheral nervous system in adult rats following systemic administration**

(A) Illustration of i.v. administration of AAV capsids MaCPNS1 and MaCPNS2 packaged with ssAAV:hSyn-tdTomato genome in a rat model (young adults, Sprague Dawley, male,  $2 \times 10^{13}$  vg/kg per rat). The rat tissues were stained with  $\alpha$ DsRed (red) antibody against tdTomato.

(B) Representative images of MaCPNS1 vector-mediated tdTomato (red) expression in major pelvic ganglia (left), sympathetic chain ganglia (middle), and inferior mesenteric ganglia (right) in adult rats 3 weeks post expression ( $n \geq 2$  per group; scale bar, 100  $\mu$ m).

(C) Representative images of MaCPNS1 vector-mediated tdTomato (red) expression in DRG (left) and TG (right). The tissues were co-stained with either  $\alpha$ NF200 (cyan),  $\alpha$ CGRP (yellow), or  $\alpha$ TRPV1 (blue) markers (scale bars, 100  $\mu$ m).

(D and E) Quantification of the proportion of AAV-mediated tdTomato expressing cells that overlap with  $\alpha$ NF200,  $\alpha$ CGRP, and  $\alpha$ TRPV1 markers in TG (above) and DRG (below), and (E) the proportion of  $\alpha$ NF200 marker+ cells that overlap with the AAV-mediated tdTomato expressing cells in DRG and TG ( $n \geq 2$  per group; each data point represents the average of at least 3 images from each rat; mean  $\pm$  SEM is plotted for  $n > 2$ ; mean is plotted for  $n = 2$ ).

(F) Representative images of MaCPNS1 and MaCPNS2 vector-mediated tdTomato expression across different segments of the GI tract: jejunum, ileum, proximal colon, and distal colon (scale bar, 200  $\mu$ m).

(G) Representative images of MaCPNS1 vector-mediated tdTomato expression in the spinal cord (above; scale bar, 500  $\mu$ m) with zoomed-in views of selected areas (white boxes; right; scale bar, 100  $\mu$ m), and the hindbrain (below; scale bar, 2 mm) with a zoomed-in view of Sp5O region (scale bar, 100  $\mu$ m). The tissues were co-stained with  $\alpha$ NeuN (blue) antibodies.

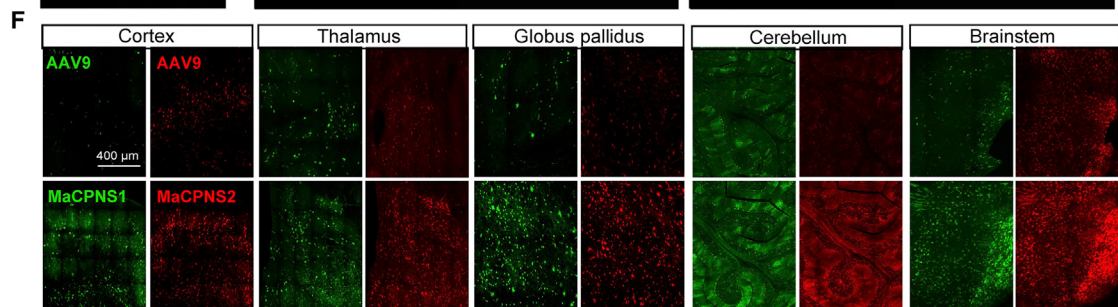
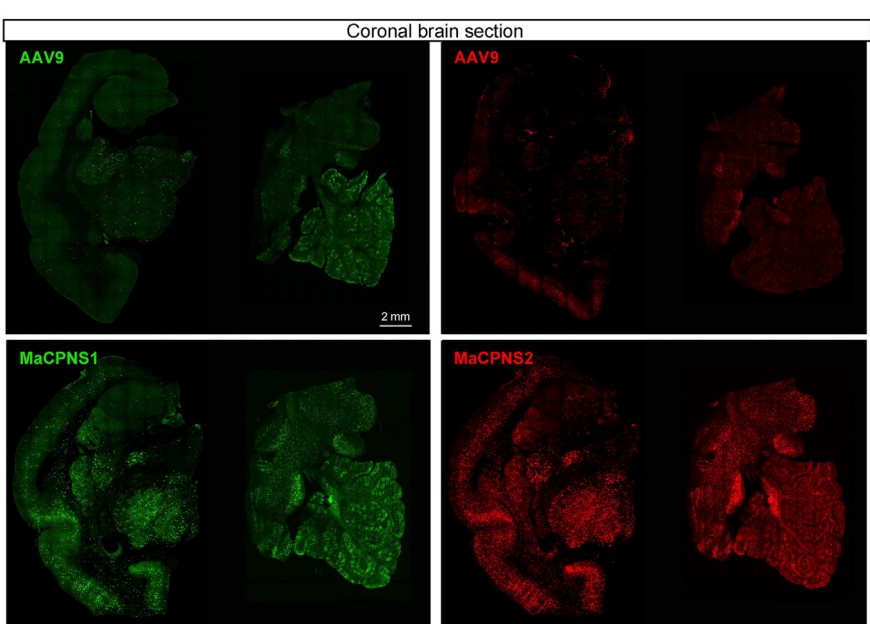
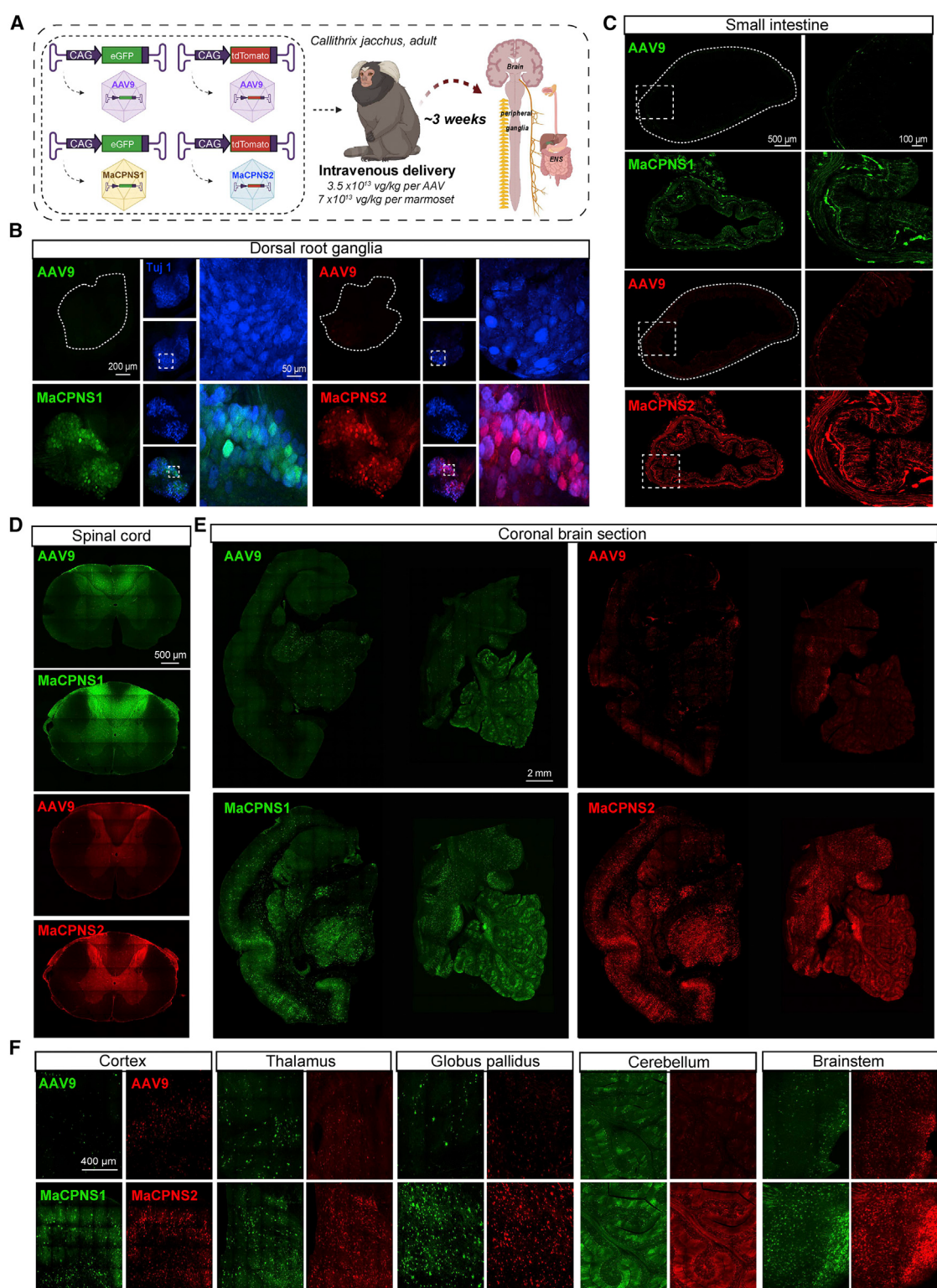


**Figure 5. Engineered AAVs can efficiently transduce the central and peripheral nervous system in marmoset**

(A–F) (A) Illustration of AAV vector delivery to adult marmoset to study transduction across the CNS and PNS after 3 weeks of expression. The capsids (AAV9/MaCPNS1/MaCPNS2) and their corresponding genomes (ssAAV:CAG-eGFP/tdTomato) are shown on the left. Two AAV vectors packaged with colored fluorescent reporters were mixed and intravenously delivered at a total dose of  $7 \times 10^{13}$  vg/kg per adult marmoset (16-month-old *Callithrix jacchus*, i.e.,  $3.5 \times 10^{13}$  vg/kg per AAV). Representative images of marmoset, (B) DRGs (scale bar, 200 μm, left and 500 μm, right), (C) small intestine (scale bar, 500 μm, left and 100 μm, right), (legend continued on next page)

A similar improvement in neuronal and astrocytic transduction was also observed in the thalamus (Figure S7C). Consistent with our observations in marmoset, MaCPNS1's transduction was more biased toward neurons, whereas MaCPNS2 showed increased transduction of both neurons and astrocytes. No significant difference in liver transduction was observed between MaCPNS1, MaCPNS2, and AAV9 (Figure S6).

These experiments demonstrate that the new capsids, MaCPNS1/2, can efficiently transduce the PNS and CNS in both New and Old World monkeys, making them useful vectors for translational research across the nervous system.

## DISCUSSION

In this study, we describe systemic AAVs that address the pressing need for efficient gene delivery vectors to target the nervous system across species. By *in vivo* selection and data analysis, we identified a library of capsids with divergent tropism compared with their parent, AAV9. Two variants, MaCPNS1 and MaCPNS2, were noteworthy for their potent neurotropic behavior in the mouse model in which they were selected. In contrast to our previously engineered PNS-targeting variant, AAV-PHP.S, which requires a high dose to be potent, i.v. delivery of a modest dose of the new variants in adult mice showed about 2-fold improvement in the transduction of NG and DRG compared with AAV9. In addition to improved sensory ganglia transduction, the MaCPNS2 capsid showed improved transduction of the SI of the ENS. These MaCPNS1/2 capsids also stood out from AAV9 and PHP.S in their specificity for the PNS, with lower transduction in the liver. In addition to their performance in adult mice, the new vectors efficiently transduced DRG when delivered at the P1 neonatal stage in mice, via a technically easy i.p. injection. In neonatal mice, both vectors showed a significant bias toward transducing CGRP+ neurons.

Experiments involving functional readout or modulation in the sensory system require a high copy number of functional proteins. This can be challenging to achieve with systemic delivery and is thought to require a combination of both an efficient vector and an engineered genetic indicator/probe (Bedbrook et al., 2019; Michelson et al., 2019; Grødem et al., 2021). In this study, we demonstrate that it is possible to use the new MaCPNS1 capsid systemically for both monitoring and modulating neuronal function. By systemically delivering a recently engineered GECI, jGCaMP8s, we were able to visualize vagal neuron calcium dynamics in response to gut glucose infusion and distension. By demonstrating the use of viral vector-mediated GECI delivery for imaging in wild-type mice, we highlight the possibility of performing similar imaging studies in species where transgenic models may not be available. Following our success with GECI sensor delivery, we extended the application of the MaCPNS1 vector to systemic delivery of a DREADD actuator to a TRPV1-Cre neonate, enabling pain induction by chemogenetic

modulation of TRPV1+ neurons in DRG, which mediate thermo-sensation and pain (Cavanaugh et al., 2011; Mishra et al., 2011; Pogorzala et al., 2013). These proof-of-concept experiments demonstrate the potential of MaCPNS1/2 for modulating different sensory modalities with higher temporal resolution. With the rapid development of ultra-sensitive opsins (Bedbrook et al., 2019; Gong et al., 2020) and a wireless light source (Yang et al., 2021), these newly developed AAV variants could potentially open the door to less invasive modulation of hard-to-access peripheral ganglia with precise temporal control.

MaCPNS1 and MaCPNS2 also show promise in rats, another commonly used research model for PNS applications (Ravagli et al., 2020; Draxler et al., 2021). Both capsids translated their potent PNS tropism across rodents, showing efficient transduction of sensory ganglia, sympathetic ganglia, parasympathetic ganglia, and enteric neurons. Detailed cell type characterization in the DRG and TG of adult rats showed that the vectors were biased toward transducing NF200+ neurons, in contrast to the bias toward CGRP+ neurons we observed in DRG in mice injected i.p. at the neonate P1 stage. Such tropism shifts have been previously noted with other AAV serotypes and emphasize the importance of considering the roles various experimental conditions play in determining a vector's tropism in a given animal model (Foust et al., 2009; Matsuzaki et al., 2018).

The conservation of the vectors' potent PNS tropism across rodents prompted us to test their performance in NHPs. First, we tested the new AAVs in a New World monkey, the marmoset, which has recently been gaining attention in the neuroscience community as a promising animal model for biomedical research (Marx, 2016; Miller et al., 2016; Jennings et al., 2016). I.v. delivery of MaCPNS1 and MaCPNS2 to adult marmosets showed potent PNS tropism. However, the vectors also efficiently crossed the BBB to transduce the CNS, making them potent vectors across the nervous system. We further validated the vectors' tropism in an Old World monkey, the rhesus macaque, which is more closely related to humans and is widely used as an animal model for pre-clinical research, including gene therapy (Jennings et al., 2016; Hudry and Vandenberghe, 2019; Bey et al., 2020). As in marmosets, i.v. delivered MaCPNS1 and MaCPNS2 efficiently transduced both the PNS and CNS in an infant rhesus macaque. The enhanced CNS tropism we observed in NHPs may be explained by the heterogeneity of the BBB across species.

The conservation of these AAV variants' potent PNS tropism across species validates the usefulness of selecting capsids in mouse models, a preferred model among capsid engineers due to the relatively fewer challenges implementing iterations of *in vivo* selection or capsid evolution given animal availability. However, the question of translatability for CNS tropism requires further investigation. Prior CNS-specific selections have yielded capsids that may or may not be translatable across species (Matsuzaki et al., 2018; Goertsen et al., 2022) or whose potential has yet to be tested.

(D) fibers in the dorsal column of the spinal cord (scale bar, 500  $\mu$ m), (E) coronal brain sections of the midbrain (left) and hindbrain (right) (scale bar, 500  $\mu$ m), and (F) select brain areas: the cortex, thalamus, globus pallidus, cerebellum, and brainstem (scale bar, 400  $\mu$ m), showing AAV9 vector-mediated expression of eGFP (green) or tdTomato (red), MaCPNS1-mediated expression of eGFP (green), and MaCPNS2-mediated expression of tdTomato (red). The images are matched in fluorescence intensity to the respective AAV9 control. Zoomed-in views of selected areas (dotted white boxes) are shown on the right in (B) and (C). In (B), the zoomed-in view shows the overlap of MaCPNS1 and MaCPNS2-mediated expression with the neuronal marker Tuj1 (blue).

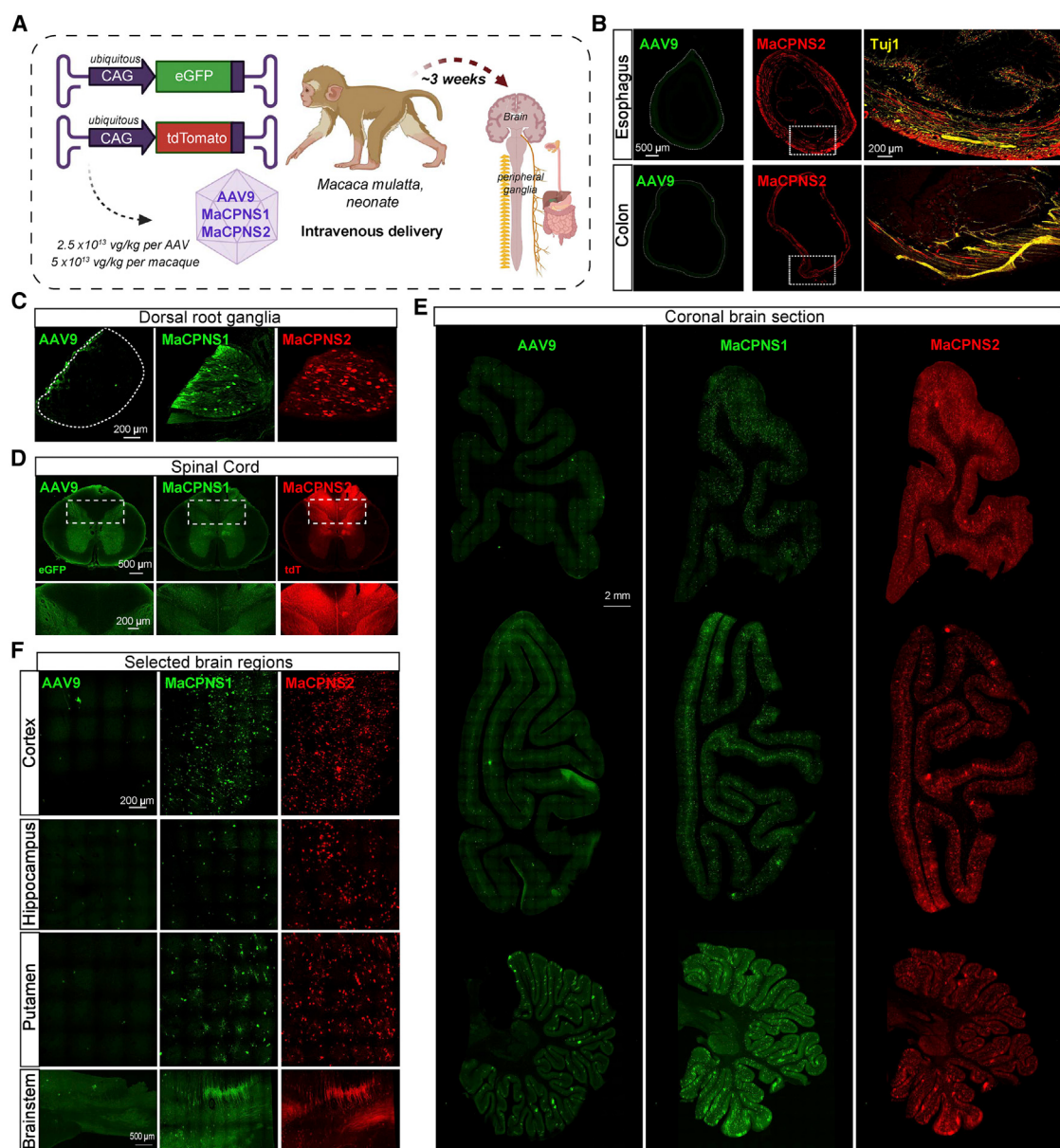


**Figure 6. Engineered variants efficiently target the central and peripheral nervous system in macaques following systemic delivery**

(A) Illustration of AAV vector delivery to macaque to study transduction across the CNS and PNS after 4 weeks of expression. The capsids (AAV9/MaCPNS1/MaCPNS2) and their corresponding genomes (ssAAV:CAG-eGFP/tdTomato) are shown on the left. Two AAVs packaged with different fluorescent proteins were mixed and intravenously injected at a dose of  $5 \times 10^{13}$  vg/kg per macaque (*Macaca mulatta*, injected within 10 days of birth, female, i.e.,  $2.5 \times 10^{13}$  vg/kg per AAV).

(B–F) Representative images of the macaque, (B) GI regions of the esophagus (top panel) and colon (bottom panel) (scale bar, 500 μm, left and 200 μm, right), (C) DRGs (scale bar, 200 μm), (D), spinal cord (scale bar, 500 μm, top and 200 μm, bottom), (E) coronal sections of forebrain, hindbrain, and cerebellum (scale bar, 2 mm), and (F) selected brain areas: cortex, hippocampus, putamen, and brainstem (scale bar, 200 μm, top and 500 μm, bottom), showing AAV9 vector-mediated expression of eGFP (green), MaCPNS1-mediated expression of eGFP (green), and MaCPNS2-mediated expression of tdTomato (red). The eGFP images of MaCPNS1 are matched in fluorescence intensity to the AAV9 control. The zoomed-in views in (B) (right) show the overlap of MaCPNS2-mediated expression of tdTomato (red) with the neuronal marker Tuj1 (yellow). The zoomed-in views in (D) (bottom) show AAV-mediated expression of eGFP (green) and tdTomato (red) in the fibers in the dorsal column (white dashed boxes).

In summary, here we introduce new AAVs to address some significant challenges in the field of gene delivery vectors for the nervous system (Table S1). Non-invasive delivery of transgenes across the nervous system can be transformative for

many applications, including basic science, as demonstrated with our previously engineered AAV vectors (Chakrabarti et al., 2020; Marvaldi et al., 2020; Reynaud-Dulaurier and Decressac, 2020; Levy et al., 2020; Takano et al., 2020; Asencor et al.,

2021; Duan et al., 2022; Monteyns et al., 2021). With several therapeutic candidates now in the pipeline for various neurological disorders (Deverman et al., 2018; Hudry and Vandenbergh, 2019; Sevin and Deiva, 2021; Privolizzi et al., 2021), the new systemic AAV vectors described in this study, AAV-MaCPNS1 and AAV-MaCPNS2, offer hope to accelerate translational research as well.

## STAR★METHODS

Detailed methods are provided in the online version of this paper and include the following:

- KEY RESOURCES TABLE
- RESOURCE AVAILABILITY

- Lead contact
  - Materials availability
  - Data and code availability

- EXPERIMENTAL MODEL AND SUBJECT DETAILS

- METHOD DETAILS

- Library plasmid preparation
  - Plasmid preparation for capsid characterization
  - AAV capsid library generation
  - *In vivo* selection and capsid library recovery
  - AAV vector production for *in vivo* characterization
  - AAV vector administration and tissue harvest in Mice
  - AAV vector administration and tissue harvest in Rat
  - AAV vector administration and tissue harvest in Marmoset
  - AAV vector administration and tissue harvest in Rhesus Macaque
  - Immunohistochemistry on tissues
  - Optical clearing for thick tissues
  - Tissue imaging and image processing
  - Nodose calcium imaging experiment
  - Pain behavior experiment
  - Analysis of pain behavior

- QUANTIFICATION AND STATISTICAL ANALYSIS

- Quantification of AAV transduction *in vivo*
  - NGS data alignment, processing and analysis
  - UMAP Clustering analysis
  - Data analysis for calcium imaging

## SUPPLEMENTAL INFORMATION

Supplemental information can be found online at <https://doi.org/10.1016/j.neuron.2022.05.003>.

## ACKNOWLEDGMENTS

We thank Yaping Lei for help with virus production; Elisha Mackey for mouse colony management; Dr. Zhe Qu and Erin Sullivan for lab management; Miguel Chuapoco for discussions on the NHP experiments; Patricia Anguiano for administrative assistance; the entire Gradinaru group and Dr. Tim Miles for discussions. We also thank Prof. Yuki Oka at Caltech for discussions on nodose calcium imaging experiments; I. Antoshechkin and the Millard and Muriel Jacobs Genetics and Genomics Laboratory at Caltech for providing sequencing service; members of the Miller lab at UCSD for performing marmoset injections and tissue collection; the staff at the California National Primate Research Center for their support with macaque experiments; and Catherine Oikonomou

for help with manuscript editing. The diagrams in the figures were created with BioRender.com.

This work was primarily supported by grants from the National Institutes of Health (NIH) to V.G.: NIH BRAIN R01MH117069, NIH Pioneer DP1OD025535, and SPARC 1OT2OD024899. Additional funding includes the following: (to V.G.) the Vallee Foundation, the Moore Foundation, the CZI Neurodegeneration Challenge Network, and the NSF NeuroNex Technology Hub grant 1707316; a grant from the Pew Charitable Trusts, the Heritage Medical Research Institute, and the Beckman Institute for CLARITY, optogenetics and vector engineering research (CLOVER) for technology development and dissemination; NIH R01 DK127257 (to I.M.C.); CZI Neurodegeneration Challenge Network (to I.M.C.); NIH R01 DC012087 (to C.T.M.); NIH P51 OD011107 (to A.S.F.); the BRAIN Initiative Armamentarium UF1MH128336 (to V.G., A.S.F., and C.T.M.); the Department of Defense grant W81XWH-17-1-0588 (to S.K.M. and V.G.); and NIH SPARC 3OT2OD023872 (to J.R.K.).

## AUTHOR CONTRIBUTIONS

X.C., S.R.K., and V.G. designed the experiments; X.C., S.R.K., C.D.A., J.R.K., D.Y., T.W., D.A.W., V.N., and L.J.C. performed the experiments; C.D.A., J.R.K., and P.B.O. assisted with the characterization of variants in rats; D.Y. and I.M.C. assisted with the characterization of the virus in pups and performed the pain experiment; T.W. and T.I. assisted with the calcium imaging experiment; D.A.W. assisted with the library selection and characterization of the virus in mice; C.M.A. assisted with the characterization of the DRG and spinal cord of NHPs; V.N. and C.T.M. assisted with the characterization of the virus in marmoset with the support of vet staff at UCSD; L.J.C. and A.S.F. assisted with the characterization of the virus in rhesus macaque with the support of staff at the California National Primate Research Center; J.A.G. and S.K.M. assisted with the characterization of the virus in mice ENS; X.C. and S.R.K. prepared the figures with input from all authors; X.C., S.R.K., and V.G. wrote the manuscript with input from all authors; V.G. supervised all aspects of the work.

## DECLARATION OF INTERESTS

The California Institute of Technology has filed and licensed patent applications for some of the work described in this manuscript, with X.C., S.R.K., and V.G. listed as inventors. V.G. is a member of the *Neuron* advisory board and a co-founder and board member of Capsida Biotherapeutics, a fully integrated AAV engineering and gene therapy company.

Received: November 9, 2021

Revised: February 18, 2022

Accepted: May 2, 2022

Published: May 27, 2022

## REFERENCES

- Ali, H.G., Ibrahim, K., Elsaied, M.F., Mohamed, R.B., Abeidah, M.I.A., Rawwas, A.O.L., Elshafey, K., Almulla, H., Akouri, K.E., et al. (2021). Gene therapy for spinal muscular atrophy: the Qatari experience. *Gene Therapy* 28, 676–680. <https://doi.org/10.1038/s41434-021-00273-7>.
- Asencor, A.I., Dvoryanchikov, G., Tsoulfas, P., and Chaudhari, N. (2021). AAV-PHP.S-mediated delivery of reporters to cranial ganglion sensory neurons. bioRxiv. <https://doi.org/10.1101/2021.09.14.460327>.
- Batista, A.R., King, O.D., Reardon, C.P., Davis, C., Shankaracharya, Philip, V., Gray-Edwards, H., Aronin, N., Lutz, C., Landers, J., et al. (2020). Ly6a differential expression in blood-brain barrier is responsible for strain specific central nervous system transduction profile of AAV-PHP. B Hum. *Gene Therapy* 31, 90–102. <https://doi.org/10.1089/hum.2019.186>.
- Bedbrook, C.N., Deverman, B.E., and Gradinaru, V. (2018). Viral strategies for targeting the central and peripheral nervous systems. *Annu. Rev. Neurosci.* 49, 323–348. <https://doi.org/10.1146/annurev-neuro-080317-062048>.
- Bedbrook, C.N., Yang, K.K., Robinson, J.E., Mackey, E.D., Gradinaru, V., and Arnold, F.H. (2019). Machine learning-guided channel rhodopsin engineering

- enables minimally-invasive optogenetics. *Nat. Methods* 16, 1176–1184. <https://doi.org/10.1038/s41592-019-0583-8>.
- Bevan, A.K., Duque, S., Foust, K.D., Morales, P.R., Braun, L., Schmelzer, L., Chan, C.M., McCrate, M., Chicoine, L.G., Coley, B.D., et al. (2011). Systemic gene delivery in large species for targeting spinal cord, brain, and peripheral tissues for pediatric disorders. *Mol. Ther.* 19, 1971–1980. <https://doi.org/10.1038/mt.2011.157>.
- Bey, K., Deniaud, J., Dubreil, L., Jousset, B., Cristini, J., Ciron, C., Hordeaux, J., Le Bouc'h, M., Marche, K., Maquigneau, M., et al. (2020). Intra-CSF AAV9 and AAVrh10 administration in nonhuman Primates: promising routes and vectors for which neurological diseases? *Mol. Ther. Methods Clin. Dev.* 17, 771–784. <https://doi.org/10.1016/j.omtm.2020.04.001>.
- Bourdenx, M., Dutheil, N., Bezzard, E., and Dehay, B. (2014). Systemic gene delivery to the central nervous system using adeno-associated virus. *Front. Mol. Neurosci.* 7, 50. <https://doi.org/10.3389/fnmol.2014.00050>.
- Cavanaugh, D.J., Chesler, A.T., Jackson, A.C., Sigal, Y.M., Yamanaka, H., Grant, R., Dajani O'Donnell, D., Nicoli, R.A., Shah, N.M., Julius, D., and Basbaum, A.I. (2011). Trpv1 reporter mice reveal highly restricted brain distribution and functional expression in arteriolar smooth muscle cells. *J. Neurosci.* Off. J. Soc. Neurosci. 31, 5067–5077. <https://doi.org/10.1523/JNEUROSCI.6451-10.2011>.
- Chakrabarti, S., Pattison, L.A., Doleschall, B., Rickman, R.H., Blake, H., Callejo, G., Heppenstall, P.A., and Smith, E.S.J. (2020). Intraarticular adeno-associated virus serotype AAV-PHP.S-mediated chemogenetic targeting of knee-innervating dorsal root ganglion neurons alleviates inflammatory pain in mice. *Arthritis Rheumatol.* 72, 1749–1758. <https://doi.org/10.1002/art.41314>.
- Challis, R.C., Ravindra Kumar, S.R., Chen, X., Goertsen, D., Coughlin, G.M., Hori, A.M., Chuapoco, M.R., Otis, T.S., Miles, T.F., and Grdinariu, V. (2022). Adeno-associated virus toolkit to target diverse brain cells. *Annu. Rev. Neurosci.* 45, 447–469. <https://doi.org/10.1146/annurev-neuro-111020-100834>.
- Challis, R.C., Ravindra Kumar, S., Chan, K.Y., Challis, C., Beadle, K., Jang, M.J., Kim, H.M., Rajendran, P.S., Tompkins, J.D., Shivkumar, K., Grdinariu, V., et al. (2019). Systemic AAV vectors for widespread and targeted gene delivery in rodents. *Nat. Protoc.* 14, 379–414. <https://doi.org/10.1038/s41596-018-0097-3>.
- Chan, K.Y., Jang, M.J., Yoo, B.B., Greenbaum, A., Ravi, N., Wu, W.-L., Sánchez-Guardado, L., Lois, C., Mazmanian, S.K., Deverman, B.E., et al. (2017). Engineered AAVs for efficient noninvasive gene delivery to the central and peripheral nervous systems. *Nat. Neurosci.* 20, 1172–1179. <https://doi.org/10.1038/nn.4593>.
- Chen, R., Canales, A., and Anikeeva, P. (2017). Neural recording and modulation technologies. *Nat. Rev. Mater.* 2, 16093. <https://doi.org/10.1038/natrevmats.2016.93>.
- Chen, W., Yao, S., Wan, J., Tian, Y., Huang, L., Wang, S., Akter, F., Wu, Yingqiu, Yao, Y., and Zhang, X. (2021). BBB-crossing adeno-associated virus vector: an excellent gene delivery tool for CNS disease treatment. *J. Control. Release* 333, 129–138. <https://doi.org/10.1016/j.jconrel.2021.03.029>.
- Corder, G., Ahanonu, B., Grewe, B.F., Wang, D., Schnitzer, M.J., and Scherrer, G. (2019). An amygdalar neural ensemble that encodes the unpleasantness of pain. *Science* 363, 276–281. <https://doi.org/10.1126/science.aap8586>.
- Deverman, B.E., Pravdo, P.L., Simpson, B.P., Kumar, S.R., Chan, K.Y., Banerjee, A., Wu, W.-L., Yang, B., Huber, N., Pasca, S.P., and Grdinariu, V. (2016). Cre-dependent selection yields AAV variants for widespread gene transfer to the adult brain. *Nat. Biotechnol.* 34, 204–209. <https://doi.org/10.1038/nbt.3440>.
- Deverman, B.E., Ravina, B.M., Bankiewicz, K.S., Paul, S.M., and Sah, D.W.Y. (2018). Gene therapy for neurological disorders: progress and prospects. *Nat. Rev. Drug Discov.* 17, 641–659. <https://doi.org/10.1038/nrd.2018.110>.
- Draxler, P., Moen, A., Galek, K., Boghos, A., Ramazanova, D., and Sandkühler, J. (2021). Spontaneous, voluntary, and affective behaviours in rat models of pathological pain. *Front. Pain Res. (Lausanne)* 2, 672711. <https://doi.org/10.3389/fpain.2021.672711>.
- Duan, Y., Ye, T., Qu, Z., Chen, Yuwen, Miranda, A., Zhou, Xiaopu, Lok, K.-C., Chen, Y., Fu, A.K.Y., Grdinariu, V., et al. (2022). Brain-wide Cas9-mediated cleavage of a gene causing familial Alzheimer's disease alleviates amyloid-related pathologies in mice. *Nat. Biomed. Eng.* 6, 168–180. <https://doi.org/10.1038/s41551-021-00759-0>.
- Foust, K.D., Nurre, E., Montgomery, C.L., Hernandez, A., Chan, C.M., and Kaspar, B.K. (2009). Intravascular AAV9 preferentially targets neonatal neurons and adult astrocytes. *Nat. Biotechnol.* 27, 59–65. <https://doi.org/10.1038/nbt.1515>.
- Giovannucci, A., Friedrich, J., Gunn, P., Kalfon, J., Brown, B.L., Koay, S.A., Taxidis, J., Najafi, F., Gauthier, J.L., Zhou, P., et al. (2019). CalmAn an open source tool for scalable calcium imaging data analysis. *eLife* 8, e38173. <https://doi.org/10.7554/eLife.38173>.
- Giusti, S.A., Vercelli, C.A., Vogl, A.M., Kolarz, A.W., Pino, N.S., Deussing, J.M., and Reijo, D. (2014). Behavioral phenotyping of Nestin-Cre mice: implications for genetic mouse models of psychiatric disorders. *J. Psychiatr. Res.* 55, 87–95. <https://doi.org/10.1016/j.jpsychires.2014.04.002>.
- Goertsen, D., Flytzanis, N.C., Goeden, N., Chuapoco, M.R., Cummins, A., Chen, Y., Fan, Y., Zhang, Q., Sharma, J., Duan, Y., et al. (2022). AAV capsid variants with brain-wide transgene expression and decreased liver targeting after intravenous delivery in mouse and marmoset. *Nat. Neurosci.* 25, 106–115. <https://doi.org/10.1038/s41593-021-00969-4>.
- Golebiowski, D., van der Bom, I.M.J., Kwon, C.-S., Miller, A.D., Petrosky, K., Bradbury, A.M., Maitland, S., Kühn, A.L., Bishop, N., Curran, E., et al. (2017). Direct intracranial injection of AAVrh8 encoding monkey β-N-acetylhexosaminidase causes neurotoxicity in the primate brain. *Hum. Gene Ther.* 28, 510–522. <https://doi.org/10.1089/hum.2016.109>.
- Gombash, S.E., Cowley, C.J., Fitzgerald, J.A., Lepak, C.A., Neides, M.G., Hook, K., Todd, L.J., Wang, G.D., Mueller, C., Kaspar, B.K., et al. (2017). Systemic gene delivery transduces the enteric nervous system of guinea pigs and cynomolgus macaques. *Gene Ther.* 24, 640–648. <https://doi.org/10.1038/gt.2017.72>.
- Gong, X., Mendoza-Halliday, D., Ting, J.T., Kaiser, T., Sun, Xuyun, Bastos, A.M., Wimmer, R.D., Guo, B., Chen, Q., Zhou, Y., et al. (2020). An ultra-sensitive step-function opsin for minimally invasive optogenetic stimulation in mice and macaques. *Neuron* 107, 38–51.e8. <https://doi.org/10.1016/j.neuron.2020.03.032>.
- Gore, R., Riedl, M.S., Kitto, K.F., Fairbanks, C.A., and Vulchanova, L. (2019). AAV-mediated gene delivery to the enteric nervous system by intracolonic injection. *Methods Mol. Biol.* 1950, 407–415. [https://doi.org/10.1007/978-1-4939-9139-6\\_24](https://doi.org/10.1007/978-1-4939-9139-6_24).
- Gray, S.J. (2016). Timing of gene therapy interventions: the earlier, the better. *Mol. Ther.* 24, 1017–1018. <https://doi.org/10.1038/mt.2016.20>.
- Gray, S.J., Woodard, K.T., and Samulski, R.J. (2010). Viral vectors and delivery strategies for CNS gene therapy. *Ther. Deliv.* 1, 517–534.
- Grødem, S., Nyemoen, I., Vatne, GuroH., Björnsdóttir, V., Lensjø, K.K., and Fyh, M. (2021). An updated suite of viral vectors for in vivo calcium imaging using local and retro-orbital injections. *bioRxiv*. <https://doi.org/10.1101/2021.05.14.443815>.
- GuhaSarkar, D., Neiswender, J., Su, Q., Gao, G., and Sena-Esteves, M. (2017). Intracranial AAV-IFN-β gene therapy eliminates invasive xenograft glioblastoma and improves survival in orthotopic syngeneic murine model. *Mol. Oncol.* 11, 180–193. <https://doi.org/10.1002/1878-0261.12020>.
- Hama, H., Hioki, H., Namiki, K., Hoshida, T., Kurokawa, H., Ishidate, F., Kaneko, T., Akagi, T., Saito, T., Saido, T., and Miyawaki, A. (2015). ScaleS: an optical clearing palette for biological imaging. *Nature Neuroscience* 18, 1518–1529. <https://doi.org/10.1038/nn.4107>.
- Hanlon, K.S., Meltzer, J.C., Buzhdyan, T., Cheng, M.J., Sena-Esteves, M., Bennett, R.E., Sullivan, T.P., Razmpour, R., Gong, Y., Ng, C., et al. (2019). Selection of an efficient AAV vector for robust CNS transgene expression. *Mol. Ther. Methods Clin. Dev.* 15, 320–332. <https://doi.org/10.1016/j.omtm.2019.10.007>.

- Hinderer, C., Katz, N., Buza, E.L., Dyer, C., Goode, T., Bell, P., Richman, L.K., and Wilson, J.M. (2018). Severe toxicity in nonhuman Primates and piglets following high-dose intravenous administration of an adeno-associated virus vector expressing human SMN. *Hum. Gene Ther.* 29, 285–298. <https://doi.org/10.1089/hum.2018.015>.
- Hirai, T., Enomoto, M., Machida, A., Yamamoto, M., Kuwahara, H., Tajiri, M., Hirai, Y., Sotome, S., Mizusawa, H., Shinomiya, K., et al. (2012). Intrathecal ShRNA-AAV9 inhibits target protein expression in the spinal cord and dorsal root ganglia of adult mice. *Hum. Gene Ther. Methods* 23, 119–127. <https://doi.org/10.1089/hgtb.2012.035>.
- Homs, J., Ariza, L., Pagès, G., Udina, E., Navarro, X., Chillón, M., and Bosch, A. (2011). Schwann cell targeting via intrasciatic injection of AAV8 as gene therapy strategy for peripheral nerve regeneration. *Gene Ther.* 18, 622–630. <https://doi.org/10.1038/gt.2011.7>.
- Hordeaux, J., Wang, Q., Katz, N., Buza, E.L., Bell, P., and Wilson, J.M. (2018). The neurotropic properties of AAV-PHP.B Are Limited to C57BL/6J mice. *Mol. Ther.* 26, 664–668. <https://doi.org/10.1016/j.ymthe.2018.01.018>.
- Hordeaux, J., Yuan, Y., Clark, P.M., Wang, Q., Martino, R.A., Sims, J.J., Bell, P., Raymond, A., Stanford, W.L., and Wilson, J.M. (2019). The GPI-linked protein LY6A drives AAV-PHP.B transport across the blood-brain barrier. *Mol. Ther.* 27, 912–921. <https://doi.org/10.1016/j.ymthe.2019.02.013>.
- Huang, L., Wan, J., Wu, Yinqiu, Tian, Y., Yao, Y., Yao, S., Ji, X., Wang, S., Su, Z., and Xu, H. (2021). Challenges in adeno-associated virus-based treatment of central nervous system diseases through systemic injection. *Life Sci.* 270, 119142. <https://doi.org/10.1016/j.lfs.2021.119142>.
- Huang, Q., Chan, K.Y., Tobey, I.G., Chan, Y.A., Poterba, T., Boutros, C.L., Balazs, A.B., Daneman, R., Bloom, J.M., Seed, C., et al. (2019). Delivering genes across the blood-brain barrier: LY6A, a novel cellular receptor for AAV-PHP.B capsids. *PLoS ONE* 14, e0225206. <https://doi.org/10.1371/journal.pone.0225206>.
- Hudry, E., and Vandenberghe, L.H. (2019). Therapeutic AAV gene transfer to the nervous system: A clinical reality. *Neuron* 101, 839–862. <https://doi.org/10.1016/j.neuron.2019.02.017>.
- Inguscio, S., Verlengia, G., Soukupova, M., Zucchini, S., and Simonato, M. (2019). Gene therapy tools for brain diseases. *Front. Pharmacol.* 10, 724. <https://doi.org/10.3389/fphar.2019.00724>.
- Jennings, C.G., Landman, R., Zhou, Y., Sharma, J., Hyman, J., Movshon, J.A., Qiu, Z., Roberts, A.C., Roe, A.W., Wang, X., et al. (2016). Opportunities and challenges in modeling human brain disorders in transgenic Primates. *Nat. Neurosci.* 19, 1123–1130. <https://doi.org/10.1038/nn.4362>.
- Jiman, A.A., Ratze, D.C., Welle, E.J., Patel, P.R., Richie, J.M., Bottorff, E.C., Seymour, J.P., Chestek, C.A., and Bruns, T.M. (2020). Multi-channel intraneuronal vagus nerve recordings with a novel high-density carbon fiber microelectrode array. *Sci. Rep.* 10, 15501. <https://doi.org/10.1038/s41598-020-72512-7>.
- Kimura, S., and Harashima, H. (2020). Current status and challenges associated with CNS-targeted gene delivery across the BBB. *Pharmaceutics* 12, 1216. <https://doi.org/10.3390/pharmaceutics12121216>.
- Kisanuki, Y.Y., Hammer, R.E., Miyazaki, J., Williams, S.C., Richardson, J.A., and Yanagisawa, M. (2001). Tie2-Cre transgenic mice: A new model for endothelial cell-lineage analysis in vivo. *Dev. Biol.* 230, 230–242. <https://doi.org/10.1006/dbio.2000.0106>.
- Körbelin, J., Dogbevia, G., Michelfelder, S., Ridder, D.A., Hunger, A., Wenzel, J., Seismann, H., Lampe, M., Bannach, J., Pasparakis, M., et al. (2016). A brain microvasculature endothelial cell-specific viral vector with the potential to treat neurovascular and neurological diseases. *EMBO Mol. Med.* 8, 609–625. <https://doi.org/10.15252/emmm.201506078>.
- Krashes, M.J., Koda, S., Ye, C.P., Rogan, S.C., Adams, A.C., Cusher, D.S., Maratos-Flier, E., Roth, B.L., and Lowell, B.B. (2011). Rapid, reversible activation of AgRP neurons drives feeding behavior in mice. *J. Clin. Invest.* 121, 1424–1428. <https://doi.org/10.1172/JCI46229>.
- Levy, J.M., Yeh, W.-H., Pendse, N., Davis, J.R., Hennessey, E., Butcher, R., Koblan, L.W., Comander, J., Liu, Q., and Liu, D.R. (2020). Cytosine and adenine base editing of the brain, liver, retina, heart and skeletal muscle of mice via adeno-associated viruses. *Nat. Biomed. Eng.* 4, 97–110. <https://doi.org/10.1038/s41551-019-0501-5>.
- Marvaldi, L., Panayotis, N., Alber, S., Dagan, S.Y., Okladnikov, N., Koppel, I., Di Pizio, A., Song, D.A., Tzur, Y., Terenzio, M., et al. (2020). Importin A3 regulates chronic pain pathways in peripheral sensory neurons. *Science* 369, 842–846. <https://doi.org/10.1126/science.aaz5875>.
- Marx, V. (2016). Neurobiology: learning from marmosets. *Nat. Methods* 13, 911–916. <https://doi.org/10.1038/nmeth.4036>.
- Masselink, W., Reumann, D., Murawala, P., Pasierbek, P., Taniguchi, Y., Bonnay, F., Meixner, K., Knoblich, J.A., and Tanaka, E.M. (2019). Broad applicability of a streamlined ethyl cinnamate-based clearing procedure. *Development* 146, dev166884. <https://doi.org/10.1242/dev.166884>.
- Matsuzaki, Y., Konno, A., Mochizuki, R., Shinohara, Y., Nitta, K., Okada, Y., and Hirai, H. (2018). Intravenous administration of the adeno-associated virus-PHP.B capsid fails to upregulate transduction efficiency in the marmoset brain. *Neurosci. Lett.* 665, 182–188. <https://doi.org/10.1016/j.neulet.2017.11.049>.
- McInnes, L., Healy, J., and Melville, J. (2020). UMAP: uniform manifold approximation and projection for dimension reduction. *Arxiv*. <http://arxiv.org/abs/1802.03426>.
- Michelson, N.J., Vanni, M.P., and Murphy, T.H. (2019). Comparison between transgenic and AAV-PHP.EB-mediated expression of GCaMP6s using in vivo wide-field functional imaging of brain activity. *Neurophotonics* 6, 025014. <https://doi.org/10.1117/1.NPh.6.2.025014>.
- Miller, C.T., Freiwald, W.A., Leopold, D.A., Mitchell, J.F., Silva, A.C., and Wang, X. (2016). Marmosets: A neuroscientific model of human social behavior. *Neuron* 90, 219–233. <https://doi.org/10.1016/j.neuron.2016.03.018>.
- Mishra, S.K., Tisel, S.M., Orestes, Peihan, Bhagoo, S.K., and Hoon, M.A. (2011). TRPV1-lineage neurons are required for thermal sensation. *EMBO J.* 30, 582–593. <https://doi.org/10.1038/emboj.2010.325>.
- Monteys, A.M., Hundley, A.A., Ranum, P.T., Tededor, L., Muehlmann, A., Lim, E., Lukashev, D., Sivasankaran, R., and Davidson, B.L. (2021). Regulated control of gene therapies by drug-induced splicing. *Nature* 596, 291–295. <https://doi.org/10.1038/s41586-021-03770-2>.
- Nonnenmacher, M., Wang, W., Child, M.A., Ren, X.Q., Huang, C., Ren, A.Z., Tocci, J., Chen, Q., Bittner, K., Tyson, K., et al. (2021). Rapid evolution of blood-brain-barrier-penetrating AAV capsids by RNA-driven biopanning. *Mol. Ther. Methods Clin. Dev.* 20, 366–378. <https://doi.org/10.1016/j.omtm.2020.12.006>.
- O'Carroll, S.J., Cook, W.H., and Young, D. (2021). AAV targeting of glial cell types in the central and peripheral nervous system and relevance to human gene therapy. *Front. Mol. Neurosci.* 13, 256. <https://doi.org/10.3389/fnmol.2020.618020>.
- Oh, S.W., Harris, J.A., Ng, L., Winslow, B., Cain, N., Mihalas, S., Wang, Q., Lau, C., Kuan, L., Henry, A.M., et al. (2014). A mesoscale connectome of the mouse brain. *Nature* 508, 207–214. <https://doi.org/10.1038/nature13186>.
- Ojala, D.S., Sun, S., Santiago-Ortiz, J.L., Shapiro, M.G., Romero, P.A., and Schaffer, D.V. (2018). In vivo selection of a computationally designed SCHEMA AAV library yields a novel variant for infection of adult neural stem cells in the SVZ. *Mol. Ther.* 26, 304–319. <https://doi.org/10.1016/j.ymthe.2017.09.006>.
- Pena, S.A., Iyengar, R., Eshraghi, R.S., Bencie, N., Mittal, J., Aljhani, A., Mittal, R., and Eshraghi, A.A. (2020). Gene therapy for neurological disorders: challenges and recent advancements. *J. Drug Target.* 28, 111–128. <https://doi.org/10.1080/1061186X.2019.1630415>.
- Piguet, F., de Saint Denis, T., Audouard, E., Beccaria, K., André, A., Wurtz, G., Schatz, R., Alves, S., Sevin, C., Zerah, M., et al. (2021). The challenge of gene therapy for neurological diseases: strategies and tools to achieve efficient delivery to the central nervous system. *Hum. Gene Ther.* 32, 349–374. <https://doi.org/10.1089/hum.2020.105>.
- Pogorzala, L.A., Mishra, S.K., and Hoon, M.A. (2013). The cellular code for mammalian thermosensation. *J. Neurosci.* 33, 5533–5541. <https://doi.org/10.1523/JNEUROSCI.5788-12.2013>.

- Privilizzi, R., Chu, W.S., Tijani, M., and Ng, J. (2021). Viral gene therapy for paediatric neurological diseases: progress to clinical reality. *Dev. Med. Child Neurol.* 63, 1019–1029. <https://doi.org/10.1111/dmcn.14885>.
- Ravagli, E., Mastitskaya, S., Thompson, N., Iacoviello, F., Shearing, P.R., Perkins, J., Gourine, A.V., Aristovich, K., and Holder, D. (2020). Imaging fascicular organization of rat sciatic nerves with fast neural electrical impedance tomography. *Nat. Commun.* 11, 6241. <https://doi.org/10.1038/s41467-020-12027-x>.
- Ravindra Kumar, S., Miles, T.F., Chen, X., Brown, D., Dobreva, T., Huang, Q., Ding, X., Luo, Y., Einarsson, P.H., Greenbaum, A., et al. (2020). Multiplexed Cre-dependent selection yields systemic AAVs for targeting distinct brain cell types. *Nat. Methods* 17, 541–550. <https://doi.org/10.1038/s41592-020-0799-7>.
- Reynaud-Dulaurier, R., and Decressac, M. (2020). PHP.B/EB vectors bring new successes to gene therapy for brain diseases. *Front. Bioeng. Biotechnol.* 8, 582979. <https://doi.org/10.3389/fbioe.2020.582979>.
- Rossi, J., Balthasar, N., Olson, D., Scott, M., Berglund, E., Lee, C.E., Choi, M.J., Lauzon, D., Lowell, B.B., and Elmquist, J.K. (2011). Melanocortin-4 receptors expressed by cholinergic neurons regulate energy balance and glucose homeostasis. *Cell Metab.* 13, 195–204. <https://doi.org/10.1016/j.cmet.2011.01.010>.
- Sevin, C., and Deiva, Kumaran. (2021). Clinical trials for gene therapy in lysosomal diseases With CNS involvement. *Front. Mol. Biosci.* 8, 624988. <https://doi.org/10.3389/fmolb.2021.624988>.
- Takano, T., Wallace, J.T., Baldwin, K.T., Purkey, A.M., Uezu, A., Courtland, J.L., Soderblom, E.J., Shimogori, T., Maness, P.F., Eroglu, C., and Soderling, S.H. (2020). Chemico-genetic discovery of astrocytic control of inhibition in vivo. *Nature* 588, 296–302. <https://doi.org/10.1038/s41586-020-2926-0>.
- Tosolini, A.P., and Smith, G.M. (2018). Editorial: gene therapy for the central and peripheral nervous system. *Front. Mol. Neurosci.* 11, 54. <https://doi.org/10.3389/fnmol.2018.00054>.
- Vogt, C.C., Bruegmann, T., Malan, D., Ottersbach, A., Roell, W., Fleischmann, B.K., and Sasse, P. (2015). Systemic gene transfer enables optogenetic pacing of mouse hearts. *Cardiovasc. Res.* 106, 338–343. <https://doi.org/10.1093/cvr/cvv004>.
- Walters, M.C., Sonner, M.J., Myers, J.H., and Ladle, D.R. (2019). Calcium imaging of parvalbumin neurons in the dorsal root ganglia. *eNeuro*. 6, 0349–18.2019. <https://doi.org/10.1523/ENEURO.0349-18.2019>.
- Williams, E.K., Chang, R.B., Strochlic, D.E., Umans, B.D., Lowell, B.B., and Liberles, S.D. (2016). Sensory neurons that detect stretch and nutrients in the digestive system. *Cell* 166, 209–221. <https://doi.org/10.1016/j.cell.2016.05.011>.
- Yang, B., Li, S., Wang, H., Guo, Y., Gessler, D.J., Cao, C., Su, Q., Kramer, J., Zhong, L., Ahmed, S.S., et al. (2014). Global CNS transduction of adult mice by intravenously delivered rAAVrh.8 and rAAVrh.10 and nonhuman primates by rAAVrh.10. *Mol. Ther.* 22, 1299–1309. <https://doi.org/10.1038/mt.2014.68>.
- Yang, Y., Wu, M., Vázquez-Guardado, A., Wegener, A.J., Grajales-Reyes, J.G., Deng, Y., Wang, Taoyi, Avila, R., Moreno, J.A., Minkowicz, S., et al. (2021). Wireless multilateral devices for optogenetic studies of individual and social behaviors. *Nat. Neurosci.* 24, 1035–1045. <https://doi.org/10.1038/s41593-021-00849-x>.
- Yardeni, T., Eckhaus, M., Morris, H.D., Huizing, M., and Hoogstraten-Miller, S. (2011). Retro-orbital injections in mice. *Lab Anim.* 40, 155–160. <https://doi.org/10.1038/laban0511-155>.
- Yu, H., Fischer, G., Ferhatovic, L., Fan, F., Light, A.R., Weihrauch, D., Sapunar, D., Nakai, H., Park, F., and Hogan, Q.H. (2013). Intraganglionic AAV6 results in efficient and long-term gene transfer to peripheral sensory nervous system in adult rats. *PLoS ONE* 8, e61266. <https://doi.org/10.1371/journal.pone.0061266>.
- Zanos, T.P., Silverman, H.A., Levy, T., Tsaava, T., Battinelli, E., Lorraine, P.W., Ashe, J.M., Chavan, S.S., Tracey, K.J., and Bouton, C.E. (2018). Identification of cytokine-specific sensory neural signals by decoding murine vagus nerve activity. *Proc. Natl. Acad. Sci. USA* 115, E4843–E4852. <https://doi.org/10.1073/pnas.1719083115>.
- Zhang, Y., Rózsa, M., Bushey, D., Zheng, J., Reep, D., Broussard, G.J., Tsang, A., Tsegaye, G., Patel, R., et al. (2020). jGCaMP8 fast genetically encoded calcium indicators. *Janelia Research Campus*. <https://doi.org/10.25378/janelia.13148243.v1>.

**STAR★METHODS**

**KEY RESOURCES TABLE**

REAGENT or RESOURCE	SOURCE	IDENTIFIER
<b>Antibodies</b>		
Rabbit anti-NeuN antibody	Abcam	Cat #ab177487; RRID:AB_2532109
Chicken anti-PGP9.5 antibody	Invitrogen	Cat #PA1-10011; RRID:AB_1088162
Goat anti-chicken Alexa647 antibody	Invitrogen	Cat #A32933; RRID: AB_2762845
Donkey anti-rabbit Alexa555 antibody	Invitrogen	Cat #A21432; RRID: AB_2535853
Rabbit anti-CGRP antibody	Millipore	Cat #PC205L; RRID: AB_2068524
Rabbit anti-Neurofilament 200 antibody	Sigma	Cat #N4142; RRID: AB_477272
Mouse anti-Tuj1 antibody	Abcam	Cat #ab7751; RRID: AB_306045
Donkey anti-rabbit DyLight488 antibody	Abcam	Cat #ab96919; RRID: AB_10679362
Donkey anti-mouse Alexa647 antibody	Abcam	Cat #ab150107; RRID: AB_2890037
Rabbit anti-dsRed antibody	Takara Bio	Cat #632496; RRID: AB_10013483
Mouse anti-Neurofilament 200 antibody	Sigma-Aldrich	Cat #N0142; RRID: AB_477257
Goat anti-calcitonin gene-related peptide antibody	Bio-Rad	Cat #1720-9007; RRID: AB_2290729
Goat anti-TRPV1 antibody	Neuromics	Cat #GT15129; RRID: AB_1624144
Donkey anti-rabbit AF594 antibody	Jackson Immuno	Cat #711-585-152; RRID: AB_2340621
Donkey anti-mouse AF488 antibody	Jackson Immuno	Cat #715-545-150; RRID: AB_2340846
Donkey anti-goat AF488 antibody	Jackson Immuno	Cat #705-545-147; RRID: AB_2336933
Mouse anti-NeuN antibody	Chemicon	Cat #MAB377; RRID: AB_2298772
Rabbit anti-S100 beta antibody	Abcam	Cat #ab52642; RRID: AB_882426
Rabbit anti-Parvalbumin antibody	Abcam	Cat #ab181086; RRID: N/A
Rabbit anti-Olig2 antibody	Abcam	Cat #ab109186; RRID: AB_10861310
Rabbit anti-GLUT1 antibody	Millipore	Cat #07-1401; RRID: AB_11212210
Goat anti-rabbit Alexa647 antibody	Invitrogen	Cat # A21245, RRID: AB_141775
<b>Experimental models: Organisms/strains</b>		
Mouse: C57BL/6J	Jackson Laboratory	Cat #000664
Mouse: Tek-Cre	Jackson Laboratory	Cat #008862
Mouse: ChAT-IRES-Cre	Jackson Laboratory	Cat #006410
Mouse: Nestin-Cre	Jackson Laboratory	Cat #003771
Mouse: TRPV1-Cre	Jackson Laboratory	Cat #017769
Mouse: TH-Cre	European Mouse Mutant Archive	Cat #EM::00254
Sprague-Dawley rat	University of Melbourne	N/A
Marmoset	University of California San Diego	N/A
Rhesus Macaque	University of California Davis	N/A
<b>Recombinant DNA</b>		
pUCmini-iCAP-AAV.MaCPNS1	In house	Deposited at Addgene #185136
pUCmini-iCAP-AAV.MaCPNS2	In house	Deposited at Addgene #185137
pAAV:hSyn1-tdTomato plasmid	Addgene	#51506
pAAV:CAG-tdTomato plasmid	Addgene	#59462
pAAV:hSyn-DIO-hM3D(Gq)-mCherry plasmid	Addgene	#44361
pGP-AAV-CAG-FLEX-jGCaMP8s-WPRE plasmid	Addgene	#162380
<b>Software and algorithms</b>		
Graphpad Prism v9	Graphpad Prism Inc	<a href="https://www.graphpad.com/scientific-software/prism/">https://www.graphpad.com/scientific-software/prism/</a>

(Continued on next page)

**Continued**

REAGENT or RESOURCE	SOURCE	IDENTIFIER
Keyence BZ-X Analyzer	Keyence	<a href="https://www.keyence.com/">https://www.keyence.com/</a>
Zen	Zeiss	<a href="https://www.zeiss.com/microscopy/us/products/microscope-software/zen.html">https://www.zeiss.com/microscopy/us/products/microscope-software/zen.html</a>
Imaris	Oxford Instruments	<a href="https://imaris.oxinst.com/">https://imaris.oxinst.com/</a>
Biorender	Biorender	<a href="https://biorender.com/">https://biorender.com/</a>
Adobe Illustrator	Adobe	<a href="https://www.adobe.com/products/illustrator/">https://www.adobe.com/products/illustrator/</a>
UMAP analysis code	McInnes, Healy, and Melville 2020	<a href="https://github.com/lmcinnes/umap">https://github.com/lmcinnes/umap</a>
CalmAn analysis code	Giovannucci et al., 2019	<a href="https://github.com/flatironinstitute/CalmAn-MATLAB">https://github.com/flatironinstitute/CalmAn-MATLAB</a>
Next generation sequencing analysis code	Ravindra Kumar et al., 2020	<a href="https://github.com/GradinaruLab/mCREATE">https://github.com/GradinaruLab/mCREATE</a>

## RESOURCE AVAILABILITY

### Lead contact

Further information and requests for resources should be directed to the [Lead Contact](#), Viviana Gradinaru ([viviana@caltech.edu](mailto:viviana@caltech.edu)).

### Materials availability

All mouse strains used in this study are available from Jackson Laboratories. All plasmids and viral vectors generated for the study have been made available from Addgene or can be obtained from the [lead contact](#) upon request. Accession numbers are listed in the key resources table.

### Data and code availability

This paper did not report original code. All data are available upon request.

## EXPERIMENTAL MODEL AND SUBJECT DETAILS

All animal procedures in mice that were carried out in this study were approved by the California Institute of Technology Institutional Animal Care and Use Committee (IACUC), and Harvard Medical School Institutional Animal Care and Use Committee (IACUC). C57BL/6J (000664), Tek-Cre (008863) (Kisanuki et al., 2001), ChAT-IRES-Cre (006410) (Rossi et al., 2011), Nestin-Cre (003771) (Giusti et al., 2014), and TRPV1-Cre (017769) (Cavanaugh et al., 2011) mice were purchased from the Jackson Laboratory (JAX). TH-Cre mice were obtained from the European Mouse Mutant Archive (EM:00254) and crossed with wild-type C57BL/6N mice. Heterozygous TH-Cre mice were used. For capsid selection experiments, 6–8 week old male and female mice were used. For *in vivo* validation studies of AAV capsid variants, 6–8 weeks old male mice were used.

All procedures performed on rats in this study were approved by the Animal Ethics Committee of the University of Melbourne (Ethics Number 1814639) and complied with the Australian Code for the Care and Use of Animals for Scientific Purposes (National Health and Medical Research Council of Australia). Six male Sprague-Dawley rats (Biomedical Sciences Animal Facility, University of Melbourne) aged 7 weeks were used in this study. Rats were housed in groups of 3 with environmental enrichment under a 12-hour (h) light-dark cycle with ad libitum access to food and water. Six male animals were used in this study and received tail vein injections of AAVs.

All experimental procedures performed on marmosets were approved by the University of California, San Diego, Institutional Animal Care and Use Committee (IACUC) and in accordance with National Institutes of Health and the American Veterinary Medical Association guidelines. 2 female animals and 1 male animal were used in this study and received intravenous injections of AAVs.

All experimental procedures performed on rhesus macaques were approved by the Institutional Animal Care and Use Committee at the University of California, Davis and the California National Primate Research Center (CNPRC). Two infant female animals were used in this study and received intravenous injections of AAVs.

For all the experiments performed in this study, the animals were randomly assigned, and the experimenters were not blinded while performing the experiments in this study unless indicated otherwise.

## METHOD DETAILS

### Library plasmid preparation

The plasmids used for AAV library preparation were described previously (Deverman et al., 2016; Ravindra Kumar et al., 2020) (plasmids available from Caltech CLOVER Center upon request). Briefly, plasmid rAAV-ΔCap-in-cis-Lox2 (Figure 1A) was used for

building the heptamer insertion (*7-mer-i*) AAV library. Plasmid pCRII-9Cap-XE was used as a PCR template for the DNA library generation. Plasmid AAV2/9-REP-AAP- $\Delta$ Cap was used to supplement the AAV library during virus production.

### Plasmid preparation for capsid characterization

The AAV capsid variants such as AAV-MaCPNS1 (Addgene plasmid # 185136) and AAV-MaCPNS2 (Addgene plasmid # 185137) capsids were built by inserting 7-mer peptides between AAs 588-589 of the AAV9 cap gene in the pUCmini-iCAP-PHP.B backbone ((Deverman et al., 2016), Addgene plasmid # 103002). The AAV-PHP.S capsid was described previously ((Chan et al., 2017), Addgene plasmid # 103006).

For *in vivo* validation of AAV capsids, we packaged the vectors with a single-stranded (ss) rAAV genome: pAAV:CAG-2xNLS-EGFP (Deverman et al., 2016) (available from Caltech CLOVER Center upon request, a similar version with 1xNLS is in Addgene, plasmid # 104061), pAAV:CAG-EGFP, pAAV:hSyn1-tdTomato (a gift from Hongkui Zeng, Addgene plasmid # 51506 (Oh et al., 2014)), pAAV:CAG-tdTomato (a gift from Edward Boyden, Addgene plasmid # 59462), pAAV:hSyn-DIO-hM3D(Gq)-mCherry (a gift from Bryan Roth, Addgene plasmid # 44361 (Krashes et al., 2011)). To make the pAAV:CAG-jGCaMP8s plasmid, jGCaMP8s was synthesized as a gBlocks Gene Fragment (IDT) based on the sequence in the plasmid pGP-AAV-CAG-FLEX-jGCaMP8s-WPRE (Addgene plasmid # 162380) and subcloned into the plasmid pAAV:CAG-EGFP by replacing the EGFP gene.

### AAV capsid library generation

The round-1 (R1) and round-2 (R2) libraries were generated as described previously (Ravindra Kumar et al., 2020). Briefly, the R1 library involved a randomized 21-nucleotide (7xNNK mutagenesis) insertion between AAs 588-589 of AAV9 capsid. The R2 library was built using a *synthetic pool* method (Ravindra Kumar et al., 2020). The R2 library was composed of an equimolar ratio of ~9000 variants that were recovered from the tissues of interest in R1 (DRG, heart, small and large intestine). The *Spike-in* variants as part of the *synthetic pool* library consisted of previously validated variants such as AAV-PHP.B, AAV-PHP.B4, AAV-PHP.C1 (CNS variants), AAV-PHP.S (PNS variant) and AAV9 parent.

### In vivo selection and capsid library recovery

For capsid selection *in vivo*, the virus library was intravenously administered to male and female mice of various Cre transgenic lines (n=2-3 per Cre line) at  $2 \times 10^{11}$  vg per mouse in R1 selection, and at  $1 \times 10^{12}$  vg per mouse in R2 selection. Two weeks post injection, mice were euthanized, the organs of interest were harvested and snap-frozen on dry ice. The tissues were stored at  $-80^{\circ}\text{C}$  for long-term. To recover capsids from the tissue, the tissues were processed using Trizol, and the rAAV genomes were recovered by Cre-dependent PCR or Cre-independent PCR as previously described (Ravindra Kumar et al., 2020). The AAV DNA library, virus library and the libraries recovered from tissue post *in vivo* selection were processed for NGS as also described previously (Ravindra Kumar et al., 2020).

### AAV vector production for *in vivo* characterization

The AAV vectors were produced using an optimized vector production protocol (Challis et al., 2019). The average yield was  $\sim 1 \times 10^{12}$  vg per plate.

### AAV vector administration and tissue harvest in Mice

For the intravenous injection procedures in mice, the AAV vectors were injected intravenously via the retro-orbital route into 6-8 week old adult mice at a dose of  $0.1\text{-}1 \times 10^{12}$  vg per mouse. The retro-orbital injections were performed as described previously (Yardeni et al., 2011; Challis et al., 2019). The expression times were  $\sim 3$  weeks from the time of injection. The dosage and expression time were kept consistent across different experimental groups unless noted otherwise.

For the intraperitoneal injection procedures in mice, neonatal pups at postnatal stage 1 (P1) were intraperitoneally injected with the AAV vectors at a dose of  $3 \times 10^{11}$  or  $1 \times 10^{12}$  vg per mouse. Six weeks after AAV administration, tissue collections were performed.

To harvest the tissues of interest, the mice were anesthetized with Euthasol (pentobarbital sodium and phenytoin sodium solution, Virbac AH) and transcardially perfused using 30 – 50 mL of 0.1 M phosphate buffered saline (PBS) (pH 7.4), followed by 30-50 mL of 4% paraformaldehyde (PFA) in 0.1 M PBS. The organs were collected and post-fixed 24-48 h in 4% PFA at  $4^{\circ}\text{C}$ . Following this, the tissues were washed with 0.1 M PBS twice and stored in fresh PBS-azide (0.1 M PBS containing 0.05% sodium azide) at  $4^{\circ}\text{C}$ .

### AAV vector administration and tissue harvest in Rat

Six 7-week-old male Sprague Dawley rats received lateral tail vein injections of either MaCPNS1 or MaCPNS2 ( $2 \times 10^{13}$  vg/kg – 3 rats/group). After a 3-week incubation period, animals were transcardially perfused with saline followed by 4% PFA, as per a published protocol (dx.doi.org/10.17504/protocols.io.bahzib76). Tissues were then dissected out and post-fixed in 4% PFA for 1 h before being washed in 0.1 M PBS (3  $\times$  30 min). Tissues were stored in PBS-azide until processing. In one rat (MaCPNS2 injection), the perfusion fixation process was unsuccessful, so tissues were fixed only by immersion (18-24 h), prior to washing and storage as described above.

### AAV vector administration and tissue harvest in Marmoset

Marmoset monkeys were anesthetized using an intramuscular Ketamine (20 mg/kg) and Acepromazine (0.5 mg/kg) injection. An intravenous catheter was placed in the saphenous vein of the hind leg and flushed with ~2 mL of LRS (Lactated Ringer's solution) for 2 min. Viruses were pooled together in a single syringe (~500-900 µL) and infused at a rate of 200 µL/min into the catheter. Following the infusion, the catheter was flushed with ~3 mL of LRS for 2 min and removed. The animal was then returned to a recovery cage.

Following an incubation period of 4-6 weeks post viral injection, the animals were euthanized by injecting pentobarbital intraperitoneally. Two researchers worked in parallel to harvest the tissue as quickly as possible to limit degradation. Each organ – brain, lungs, kidneys, etc - was removed and separated into two parts. One half of the tissue was flash-frozen in 2-methylbutane that was chilled with dry ice to preserve mRNA and DNA in the harvested tissues. The other half of the tissue was fixed in 4% PFA solution for estimation of protein expression. Flash-frozen tissue samples were transferred to a -80°C freezer, while PFA-fixed tissue samples were stored in a 4°C fridge.

### AAV vector administration and tissue harvest in Rhesus Macaque

Two female rhesus macaques were injected within 10 days of birth. Prior to injection, animals were anesthetized with ketamine (0.1 mL) and the skin over the saphenous vein was shaved and sanitized. AAVs ( $2.5 \times 10^{13}$  vg/kg) were slowly infused into the saphenous vein for ~1 min in < 0.75 mL of 0.1 M PBS. Animals were monitored while they recovered from anesthesia in their home enclosure, and daily for the remainder of the study. Monkeys were individually housed within sight and sound of conspecifics.

Tissues were collected 4 weeks post AAV administration. Animals were deeply anesthetized and euthanized using sodium pentobarbital in accordance with guidelines for humane euthanasia of animals at the CNPRC. The whole body was perfused with ice cold RNase-free 0.1 M PBS. Brains were removed from the skull and blocked into 4 mm thick slabs in the coronal plane. Brain slabs and organs were subsequently post-fixed in 4% PFA for 48 h. One hemisphere of each animal was cryoprotected in 10%, 15%, and 30% sucrose in 0.1 M PBS.

### Immunohistochemistry on tissues

In mice and NHP experiments, tissue sections, typically 100-µm thick, were first incubated in blocking buffer (10% normal donkey serum (NDS), 0.1% Triton X-100, and 0.01% sodium azide in 0.1 M PBS, pH 7.4) with primary antibodies (rabbit anti-NeuN (Abcam ab177487, 1:500), chicken anti-PGP9.5 (Invitrogen PA1-10011, 1:500), rabbit anti-S100 beta (Abcam ab52642, 1:200), rabbit anti-Parvalbumin (Abcam 181086, 1:200), rabbit anti-Olig2 (Abcam ab109186, 1:200), rabbit anti-GLUT1 (Millipore 07-1401, 1:200)) at appropriate dilutions for 24 h at room temperature (RT) on a rocker. After primary antibody incubation, the tissues were washed 1-3 times with wash buffer 1 (0.1% Triton X-100 in 0.1 M PBS buffer, pH 7.4) over a period of 5-6 h in total. The tissues were then incubated in blocking buffer with secondary antibodies (goat anti-chicken Alexa647 (Invitrogen, A32933, 1:1000), donkey anti-rabbit Alexa555 (Invitrogen, A21432, 1:1000), goat anti-rabbit Alexa647 (Invitrogen, A21245, 1:1000) at appropriate dilutions for 12-24h at RT and then washed 3 times in 0.1 M PBS over a total duration of 5-6 h. When performing DNA staining, the tissues were incubated with 4',6-Diamidino-2'-phenylindole dihydrochloride (DAPI) (Sigma Aldrich, 10236276001, 1:1000) in 0.1 M PBS for 15 min followed by a single wash for 10 min in 0.1 M PBS. The DAPI and/or antibody-stained tissue sections were mounted with ProLong Diamond Antifade Mountant (ThermoFisher Scientific, P36970) before imaging under the microscope.

For immunostaining of DRG in mice neonates and the pain induction experiment, DRGs from spinal cord segments: thoracic levels 11-13 and lumbar levels 1-5 or 1-6 were dissected, fixed for 2 h in 4% PFA (diluted in 0.1 M PBS) at 4°C, incubated overnight at 4°C in 30% sucrose solution (diluted in 0.1 M PBS), and embedded in OCT (Tissue-Tek®). Sections of 14 µm thickness were cut and blocked with blocking buffer-1 (10% NDS, in PBST solution containing 0.3% Triton X-100 and 0.1 M PBS, pH 7.4) for 2 h at RT. Tissues were stained with primary antibodies (rabbit anti-CGRP (Millipore PC205L, 1:500), rabbit anti-Neurofilament 200 (Sigma N4142, 1:500), mouse anti-Tuj1 (Abcam ab7751, 1:1,000)) that were diluted in blocking buffer-2 (2% NDS in PBST solution) and incubated overnight at 4°C. Sections were washed in PBST buffer, then stained with secondary antibodies (donkey anti-rabbit DyLight488 (Abcam ab96919, 1:1000), donkey anti-mouse Alexa647 (Abcam ab150107, 1:500)) diluted in blocking buffer-2 for 2 h at RT. After washing with 0.1 M PBS, sections were mounted in VectaShield (Vector Labs), and imaged in an Olympus Fluoview 1000 confocal microscope with 20X magnification at HMS Microscopy Resources on the North Quad (MicRoN) Core. Five DRG images per mouse were used for quantification.

To immunostain rat organs and sensory ganglia, cryosections (14 µm) mounted onto gelatinized slides were washed in PBS (1 × 10 min) followed by 1 h incubation in blocking solution (PBS containing 0.1% Triton X-100 and 10% horse serum). Sections were incubated with primary antibody (hypertonic PBS, 18-24 h in a humid chamber), washed in PBS (1 × 15 min) and incubated with secondary antibody (2 h). Sections were again washed in PBS (1 × 15 min) and then coverslipped using buffered glycerol. This method is described in detail in [dx.doi.org/10.17504/protocols.io.w3ffgjn](https://dx.doi.org/10.17504/protocols.io.w3ffgjn). DRG and trigeminal tissue were labelled for DsRed and each of the 3 markers (NF-200, CGRP, TRPV1) while liver tissue was labelled for DsRed and DAPI. Primary antibodies were: rabbit anti-dsRed (Takara Bio, 632496, 1:5000); mouse anti-neurofilament 200 (Sigma-Aldrich, N0142, 1:4000); goat anti-calcitonin gene-related peptide, Bio-Rad, 1720-9007, 1:5000; goat anti-TRPV1 (Neuromics, GT15129, 1:1000). Secondary antibodies were: donkey anti-rabbit AF594 (Jackson ImmunoResearch Laboratories, 711-585-152, 1:1000); donkey anti-mouse AF488 (Jackson, 715-545-150, 1:2000); donkey anti-goat AF488 (Jackson, 705-545-147, 1:1000).

To immunostain rat CNS, cryosections (40 µm) of brain (coronal) and L4-L5 spinal cord (transverse) were collected in a 1 in 4 series and stored in PBS-azide until use. Sections were washed in PBS (3 × 10 min) followed by 2 h incubation in blocking solution (PBS containing 0.5% Triton X-100 and 10% horse serum), washed in PBS (3 × 10 min) then incubated for 48 h with primary antibody (0.1% PBS-azide containing 0.5% Triton X-100 and 2% horse serum). Tissues were then washed in PBS (3 × 10 min) followed by 4 h incubation with secondary antibody. Tissues were washed in PBS (3 × 10 min) and then mounted and coverslipped using buffered glycerol. This method is described in detail in ([dx.doi.org/10.17504/protocols.io.bakkicuw](https://dx.doi.org/10.17504/protocols.io.bakkicuw)). Primary antibodies used were: rabbit anti-dsRed (Takara Bio, 632496, 1:5000) and mouse anti-NeuN (Chemicon, MAB377, 1:2000). Secondary antibodies are described above.

To immunostain whole mounts of autonomic ganglia (IMG, MPG, sympathetic chain) and intestine, tissues were washed in PBS (3 × 30 min) followed by 2 h incubation in blocking solution (PBS containing 0.5% Triton X-100 and 10% horse serum). Tissues were again washed in PBS (3 × 30 min) before 72 h incubation with primary antibody (0.1% PBS-Azide containing 0.5% Triton X-100 and 2% horse serum). Tissues were then washed in PBS (3 × 30 min) followed by 24 h incubation with secondary antibody. Tissues were washed in PBS (3 × 30 min) before being cleared using ethyl cinnamate ([Masselink et al., 2019](#)). Briefly, tissues were washed in methanol (100%, 3 × 30 min) followed by dichloromethane (1 × 30 min) and then ethyl cinnamate (2 × 30 min). Tissues were then mounted on glass slides and coverslipped using ethyl cinnamate.

### Optical clearing for thick tissues

For imaging tissues >100 microns in thickness such as gut, optical clearing was carried out by incubating small pieces (0.5–1 cm length) of tissue in 1–2 mL of ScaleS4(0) ([Hama et al., 2015](#)) solution overnight at RT with gentle agitation. The tissues were then mounted in fresh ScaleS4(0) solution with spacers (0.1–1 mm thick) on glass slides and imaged under the microscope.

### Tissue imaging and image processing

The images used in this study were acquired with a Zeiss LSM 880 confocal microscope using the following objectives: Plan-Apo-chromat 10X 0.45 M27 (working distance 2.0 mm), and Plan-Apochromat 25X 0.8 Imm Corr DIC M27 multi-immersion. The liver images were acquired with a Keyence BZ-X700 microscope using a 20X objective. The images were then processed in the following image processing software: Zen Black 2.3 SP1 (for Zeiss confocal images) and BZ-X Analyzer (for Keyence images).

Image collection and analysis for cryosections of rat sensory ganglia and organs was performed using wide-field fluorescence microscopy with an ApoTome attachment (Zeiss AxioImager M2). Quantification of AAV+ and AAV+/Marker+ neurons was performed for DRG and trigeminal ganglia on 4 non-sequential sections with only nucleated neuronal profiles counted. Counts were performed manually while viewing sections under the microscope. For CNS sections and whole mounts of intestine and ganglia, image collection and analysis was performed using wide-field fluorescence microscopy with an ApoTome attachment (Zeiss AxioImager M2).

### Nodose calcium imaging experiment

*In vivo* vagal ganglion imaging was conducted as previously described ([Williams et al., 2016](#)). Briefly, animals were anesthetized with pentobarbital at a dose of 100 mg/kg body weight, injected intraperitoneally (i.p.). A skin incision was made to expose the abdominal region. For intestinal glucose infusion and distension, an input tubing (HelixMark Silicone Tubing 60-011-04) was inserted in the jejunum and the output tubing (HelixMark Silicone Tubing 60-011-09) was set at the ileum. Surgical thread was used to fasten and secure tubing sites. During the abdominal surgery, isotonic saline was applied occasionally to prevent tissue drying. After suturing the abdominal region, a midline neck incision was made. Muscles were separated and retracted laterally to expose the trachea and vagus trunk. To free the vagal ganglion, the carotid artery was retracted aside, and the vagus nerve was transected superior to the jugular ganglion. The vagal ganglion was then placed on a custom 5-mm diameter glass coverslip (72290-01, Electron Microscopy Sciences), and immediately immersed in silicon adhesive (Kwik-SIL, World Precision Instruments). Imaging was conducted with a Leica SP8 confocal microscope, with a frame rate of 1 Hz. For glucose stimulus, 300 mM glucose solution was infused at a flow rate of 800 µL/min for 2 min. Intestinal distension stimulus was achieved by closing the exit port for 1 min while infusing saline.

### Pain behavior experiment

TRPV1-Cre neonatal pups at postnatal stage 1 (P1) were intraperitoneally injected with 10 µL of MaCPNS1:Syn-DIO-hM3D(Gq)-mCherry virus ( $3 \times 10^{13}$  vg/ml). Six weeks after injection, mice were subjected to a pain test in an infrared Behavior Observation Box (iBOB) (Harvard Apparatus) which allowed video recording of mice in the dark and independent of an observer. Prior to Clozapine-N-oxide (CNO) injection, mice were habituated for 30 min in individual chambers of the iBOB. Mice were then given intraplantar injection of 10 µL of CNO or vehicle (5% Dimethyl sulfoxide (DMSO) in 0.1 M PBS). Injections were performed under light restraint without anesthesia. Mice were immediately placed in the iBOB and recorded. Total bouts of lifting/licking of the footpad and total time spent licking/lifting the footpad for the first 15 minutes after CNO injection were quantified.

### Analysis of pain behavior

The 20-min videos recorded in the pain-induction experiment were scored by a blinded observer to quantify the total bouts and time spent licking and shaking the injected paw within 15 min. GraphPad Prism was used for statistical comparison and plotting.

## QUANTIFICATION AND STATISTICAL ANALYSIS

### Quantification of AAV transduction *in vivo*

The quantification of AAV transduction across NG, DRG and GI tract was carried out by manually counting fluorescent expression resulting from the AAV genome. The Adobe Photoshop CC 2018 Count Tool was used for this purpose. To quantify expression in the liver, we used Keyence Analyzer automated cell count software. The efficiency was determined by the percentage of cells expressing EGFP or tdTomato relative to a specific cell marker, namely, NeuN, PGP9.5, DAPI, CGRP, NF200, TRPV1, Tuj1, GLUT1, Olig2 or S100 $\beta$ .

### NGS data alignment, processing and analysis

The raw fastq DNA files were aligned to the AAV9 capsid template using custom alignment software as described previously (Ravindra Kumar et al., 2020) (<https://github.com/GradinaruLab/mCREATE>). The NGS data analysis was carried out using a custom data-processing pipeline with scripts written in Python (<https://github.com/GradinaruLab/mCREATE>) and plotting software such as Plotly, Seaborn, and GraphPad PRISM 7.05. The AAV9 capsid structure model was produced with PyMOL.

The enrichment score for a variant was determined using the following formula:

Enrichment score of variant “x” =  $\log_{10} [(\text{Variant } "x" \text{ RC in tissue library1} / \text{Sum of variants N RC in library1}) / (\text{Variant 1 RC in virus library} / \text{Sum of variants N RC in virus library})]$

Where N is the total number of variants in a library.

The fold-change of a variant “x” to AAV9 = (The enrichment of “x”-The enrichment of AAV9)/|The enrichment of AAV9|.

### UMAP Clustering analysis

For profiling the overall tropism of the AAV library post R2 selection, a non-linear algorithm, UMAP (McInnes et al., 2020), was used for dimension reduction and visualization with a script adapted from <https://github.com/lmcinnes/umap>. After the M-CREATE data-processing pipeline, the R2 capsid library yielded enrichment scores across 22 targets (tissues; Figure 1B). These enrichment scores served as 22 dimensions that were fed into the UMAP algorithm, and the parameters considered were n\_neighbors (15), n\_components (2), random\_state (42), distance\_metric ('correlation'), verbose (3).

### Data analysis for calcium imaging

Imaging data was analyzed using CalmAn-MATLAB (Giovannucci et al., 2019; Corder et al., 2019) with modified MATLAB code adapted from <https://github.com/flatironinstitute/CalmAn-MATLAB>. Basically, imaging frames from the same animal were first registered to correct for motion. A non-negative matrix factorization (CNMF) algorithm was applied to recognize individual cells and to extract fluorescence activities. A 30 s window before the stimulus onset was used as baseline signal. To quantify signals, the mean ( $\mu$ ) and standard deviation ( $\sigma$ ) of  $F_0(t)$  over the baseline period were computed as  $F(t) = (F_0(t) - \mu)/\sigma$ . Cells were defined as responsive if the average  $\Delta F/F(\sigma)$  value during the stimulus period was more than 3 s.d. above the baseline mean activity.

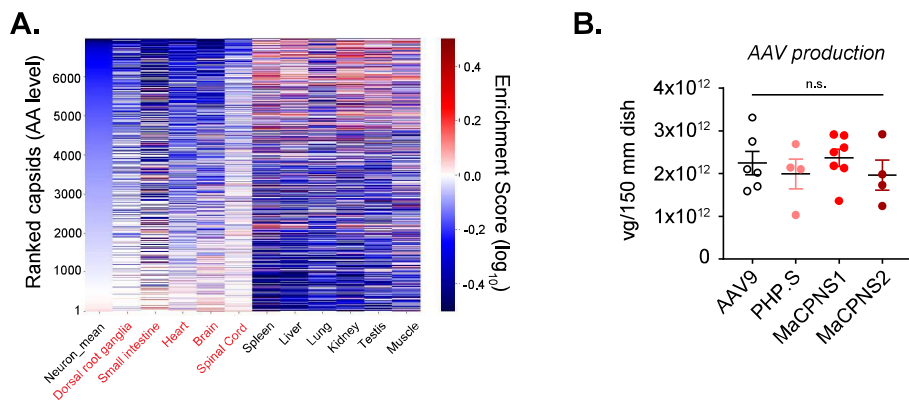
**Supplemental information**

**Engineered AAVs for non-invasive gene delivery**

**to rodent and non-human primate nervous systems**

**Xinhong Chen, Sripriya Ravindra Kumar, Cameron D. Adams, Daping Yang, Tongtong Wang, Damien A. Wolfe, Cynthia M. Arokiaraj, Victoria Ngo, Lillian J. Campos, Jessica A. Griffiths, Takako Ichiki, Sarkis K. Mazmanian, Peregrine B. Osborne, Janet R. Keast, Cory T. Miller, Andrew S. Fox, Isaac M. Chiu, and Viviana Gradinaru**

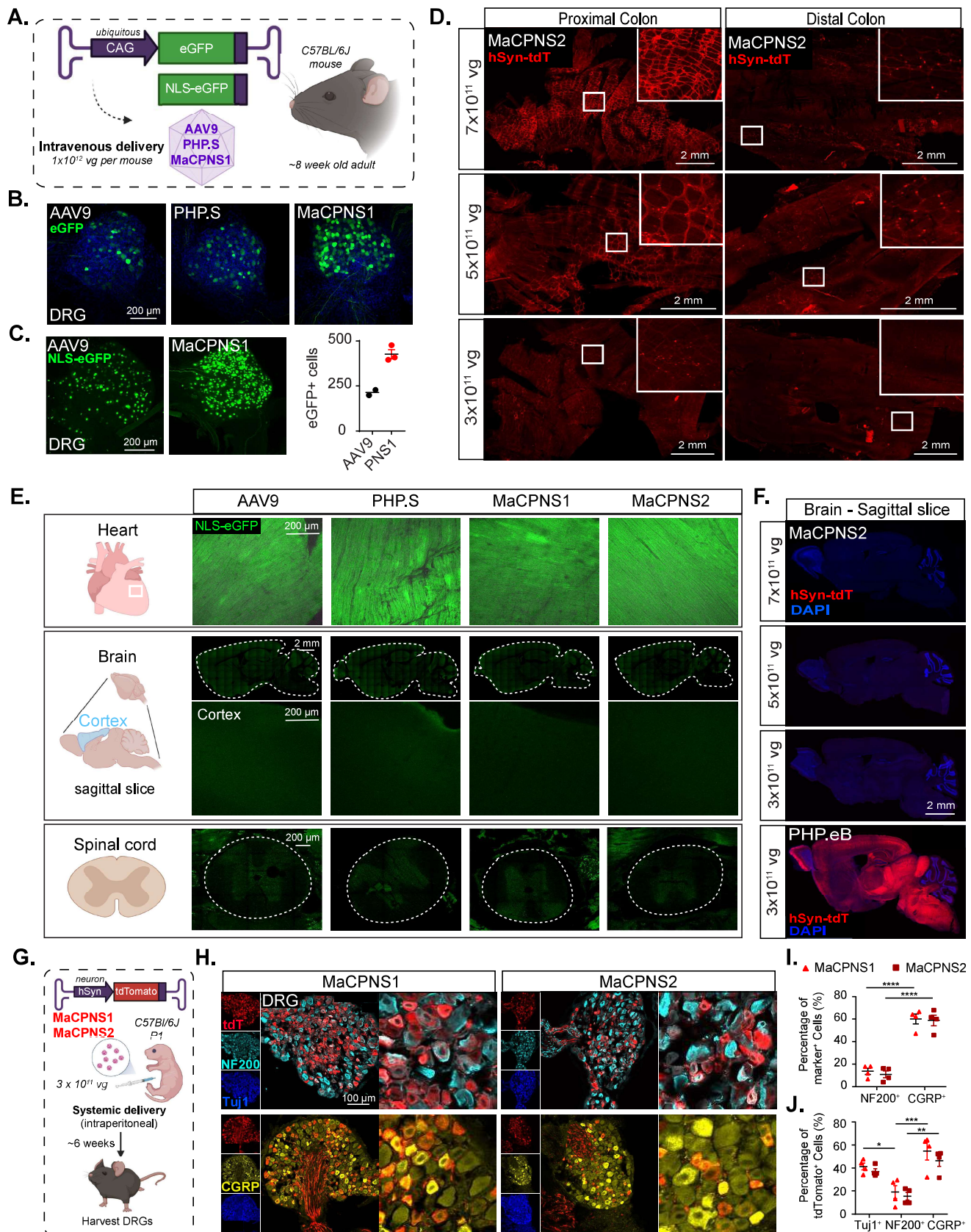
Supplementary Figure 1: AAV capsid library outcome post round-2 *in vivo* selection



**Supplementary Figure 1: AAV capsid library outcome post round-2 *in vivo* selection.  
Related to Figure 1.**

**A.** Heatmap of 6300 capsid variants which showed a bias towards one or more of the neuronal tissues. Heatmap shows mean enrichment by Cre-dependent recovery across tissues of interest (red text) and Cre-independent recovery across off-targets (black text) after two rounds of selection. Cre lines are grouped by organs. The y-axis represents capsids unique at the amino acid (AA) level, ranked by ‘neuron mean’, which is the mean of the enrichment of all targets of interest. **B.** AAV vector yields from an established laboratory protocol (see Methods). One-way analysis of variance (ANOVA) non-parametric Kruskal-Wallis test (approximate  $P=0.6407$ , n.s.), and follow-up multiple comparisons with uncorrected Dunn’s test are reported (individual  $P > 0.05$ , n.s.;  $n \geq 4$  per group, each data point is the mean of 3 technical replicates, mean  $\pm$  s.e.m is plotted).

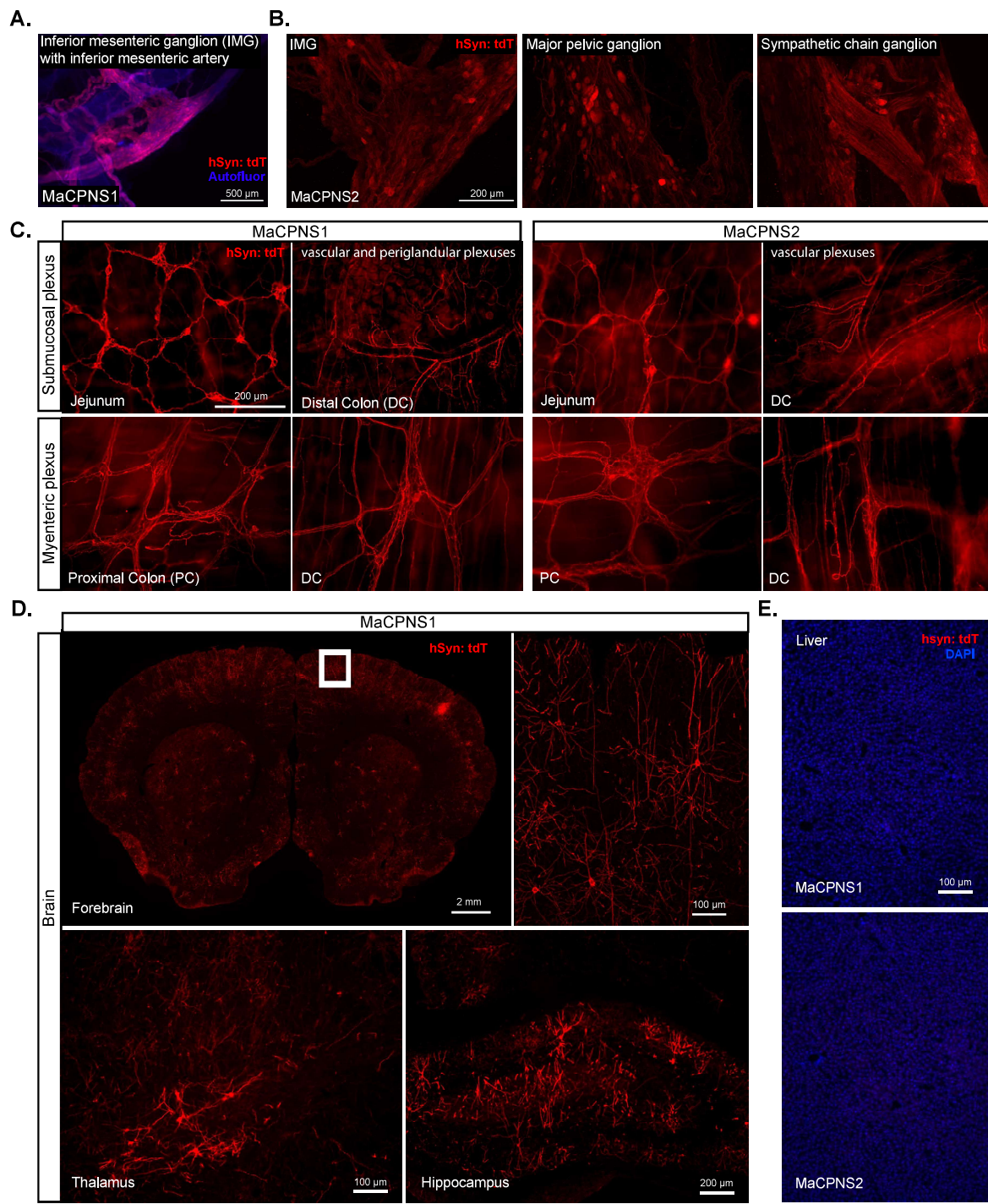
Supplementary Figure 2: Characterization of AAV variants across different organs in mice following systemic delivery.



**Supplementary Figure 2: Characterization of AAV variants across different organs in mice following systemic delivery. Related to Figure 2.**

**A.** Illustration of IV administration of AAV9/PHP.S/MaCPNS1 capsid packaged with either ssAAV:CAG-eGFP or ssAAV:CAG-NLS-eGFP genome in mice (~8 weeks old, C57BL/6J males) at  $1 \times 10^{12}$  vg dose/mouse. **B.** Vector (AAV9/PHP.S/MaCPNS1)-mediated expression of eGFP (green) in DRG after 3 weeks of expression *in vivo* (n=3 per group). **C.** Vector-mediated expression of NLS-eGFP (green) in DRG after 3 weeks of expression, with imaging parameters matched across samples. Quantification of eGFP+ cells in DRG is shown at right (n=2-3 per group, mean  $\pm$  s.e.m is plotted for n>2, mean is plotted for n=2). **D.** MaCPNS2 vector-mediated expression of tdTomato (red) from ssAAV:hSyn-tdTomato in the proximal and distal segments of the colon at three different IV doses per mouse:  $7 \times 10^{11}$  vg,  $5 \times 10^{11}$  vg,  $3 \times 10^{11}$  vg (3 weeks of expression, n=3 per group, white boxes show zoomed-in views of selected areas). **E.** Vector (AAV9, PHP.S, MaCPNS1 and MaCPNS2)-mediated expression of NLS-eGFP (green) in organs after 3 weeks of expression. Top panels show expression in heart. Middle panels show expression in the brain with zoomed-in views of the cortex. Bottom panels show expression in the spinal cord. **F.** MacPNS2 vector-mediated expression of tdTomato (red) from ssAAV:hSyn-tdTomato in the brain at three different IV doses per mouse:  $7 \times 10^{11}$  vg,  $5 \times 10^{11}$  vg,  $3 \times 10^{11}$  vg (3 weeks of expression, n=3 per group). Bottom panel shows PHP.eB vector-mediated expression of tdTomato (red) using ssAAV:hSyn-tdTomato in the brain at an IV dose per mouse of  $3 \times 10^{11}$  vg (3 weeks of expression, n=3 per group). The tissues were co-stained with the nuclear stain DAPI (blue). Imaging parameters in **B-F** were matched across samples to the respective control in the experiment or the area. **G.** Illustration of intraperitoneal administration of MaCPNS1 vector packaged with ssAAV:hSyn-tdTomato in a C57BL/6J mouse model (postnatal stage 1 (P1), males,  $3 \times 10^{11}$  vg IV dose/mouse). After six weeks of expression, the DRG were harvested. **H.** Representative images of DRG sections showing MaCPNS1 vector-mediated tdTomato (red) expression. The tissues were co-stained with  $\alpha$ NF200 (cyan),  $\alpha$ Tuj1 (blue) and  $\alpha$ CGRP (yellow) markers. **I.** Quantification of the proportion of  $\alpha$ NF200 and  $\alpha$ CGRP marker+ cells that overlap with the AAV-mediated tdTomato-expressing cells in DRG, and **J.** proportion of AAV-mediated tdTomato-expressing cells that overlap with  $\alpha$ Tuj1,  $\alpha$ NF200 and  $\alpha$ CGRP markers in DRG (n=4 per group, unpaired t-test. Mean $\pm$  sem are shown.)

Supplementary Figure 3: Novel variants transduce peripheral ganglia and CNS in rats.

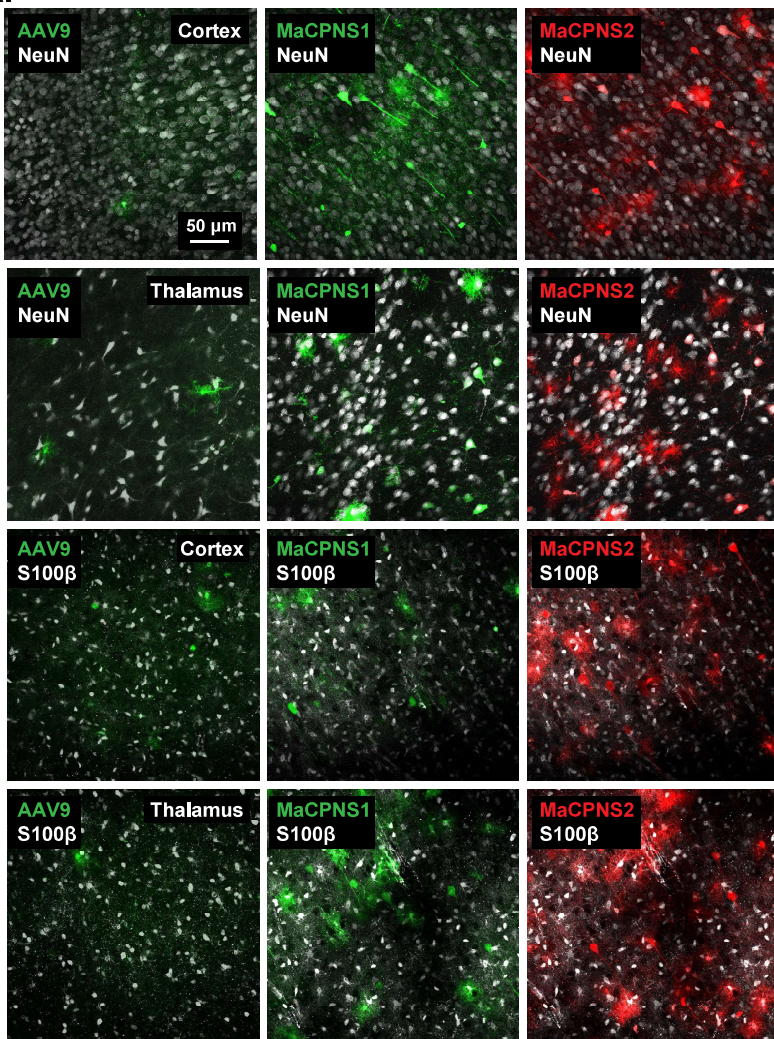


**Supplementary Figure 3. Novel variants transduce peripheral ganglia and CNS in rats.  
Related to Figure 3.**

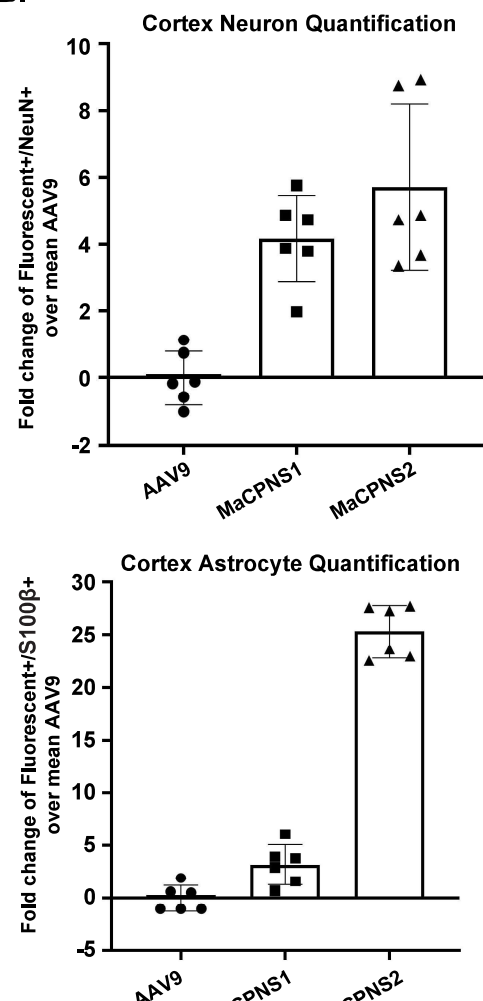
AAV capsids (MaCPNS1 and MaCPNS2 packaged with ssAAV:hSyn-tdTomato genome) were intravenously administered in a rat model (young adults, Sprague Dawley, male,  $2 \times 10^{13}$  vg/kg per rat). The tissues were stained with  $\alpha$ DsRed (red) antibody against tdTomato. **A.** Representative image of MaCPNS1 vector-mediated tdTomato (red) expression in inferior mesenteric ganglion with inferior mesenteric artery (scale bar: 500  $\mu$ m). **B.** Representative images of MaCPNS2 vector-mediated tdTomato (red) expression in major pelvic ganglia (left), sympathetic chain ganglia (middle) and inferior mesenteric ganglia (right) in adult rats after 3 weeks of expression ( $n \geq 2$  per group, scale bar: 200  $\mu$ m). **C.** Representative images of MaCPNS1 (left) and MaCPNS2 (right) vector-mediated tdTomato expression in the jejunum and distal colon at the submucosal plexus layer (top) and proximal colon and distal colon at the myenteric plexus layer (bottom). (scale bar: 200  $\mu$ m). **D.** Representative images of MaCPNS1 vector-mediated tdTomato expression in the brain including forebrain (top left, scale bar: 2mm) with zoomed-in view of the cortex (white box, scale bar: 100  $\mu$ m), thalamus (bottom left, scale bar: 100  $\mu$ m) and hippocampus (bottom right, scale bar: 200  $\mu$ m). **E.** Representative images of MaCPNS1 and MaCPNS2 vector-mediated tdTomato expression in the liver. The tissues were co-stained with DAPI (blue) (scale bar: 100  $\mu$ m).

Supplementary Figure 4: Cell-type profiles of engineered AAVs in marmoset brain

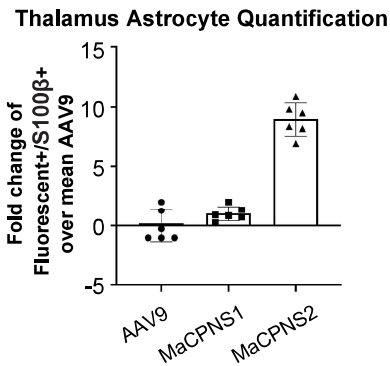
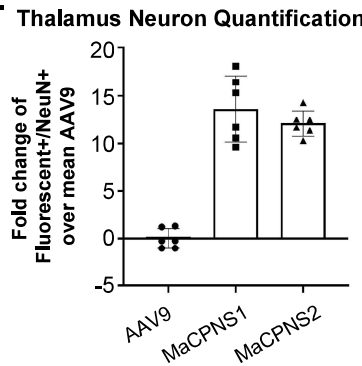
A.



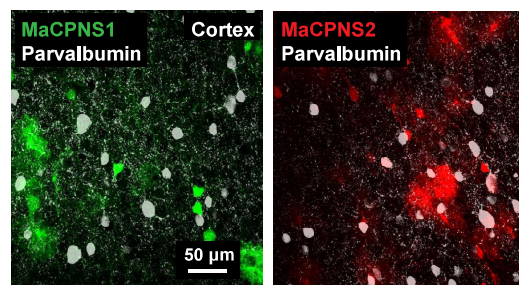
B.



C.



D.

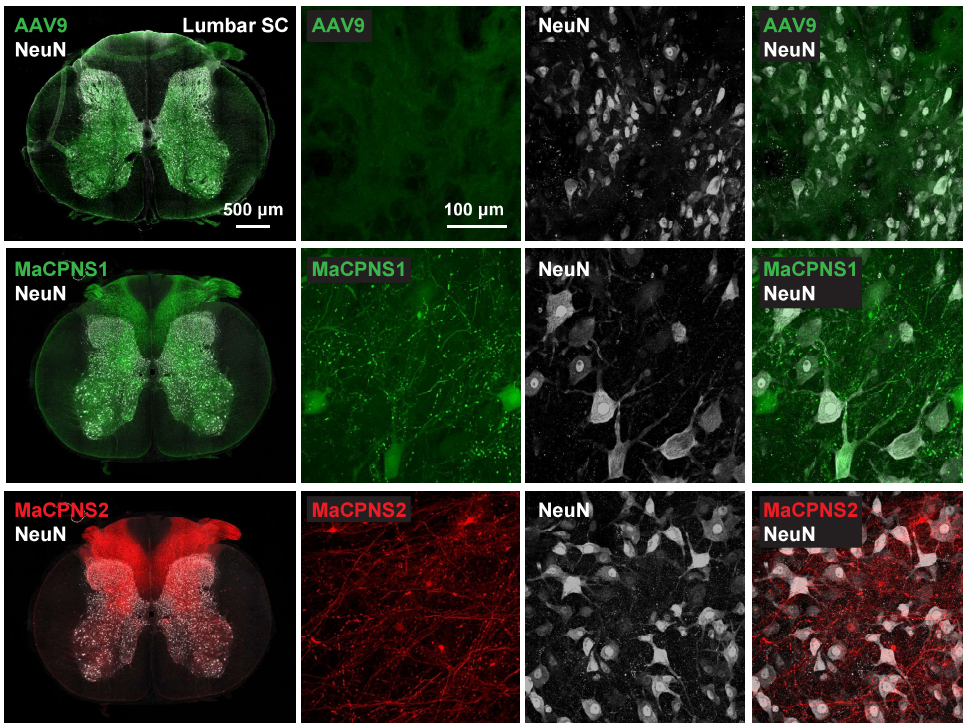


**Supplementary Figure 4. Cell-type profiles of engineered AAVs in marmoset brain.  
Related to Figure 5.**

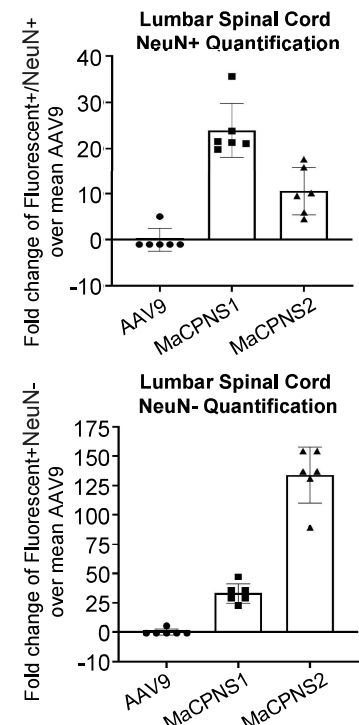
**A.** Representative images of AAV9, MaCPNS1 and MaCPNS2 vector-mediated fluorescent protein expression in the marmoset cortex and thalamus (scale bar: 50  $\mu$ m). Slices were co-stained with NeuN (top 2 rows, white) or S100 $\beta$  (bottom 2 rows, white). **B, C.** Quantification of the fold change of Fluorescent+/marker over mean AAV9 in cortex and thalamus. Each data point is a slice. **D.** Representative images of MaCPNS1 and MaCPNS2 vector-mediated fluorescent protein expression in the marmoset cortex (scale bar: 50  $\mu$ m). Slices were co-stained with Parvalbumin (white).

Supplementary Figure 5 : Engineered vectors transduce spinal cord and DRG in macaque efficiently

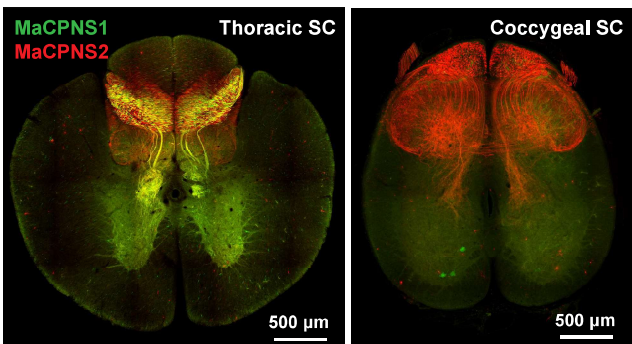
**A.**



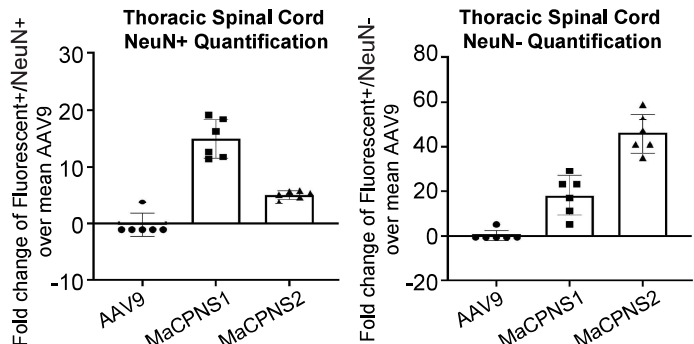
**B.**



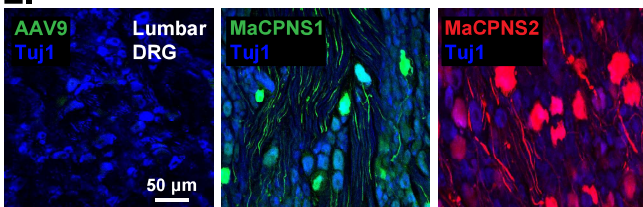
**C.**



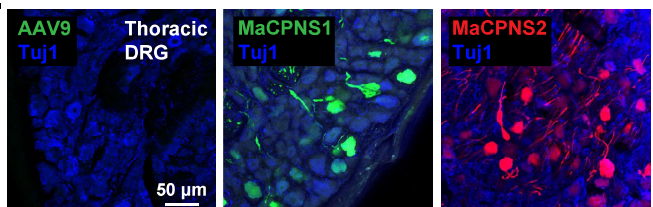
**D.**



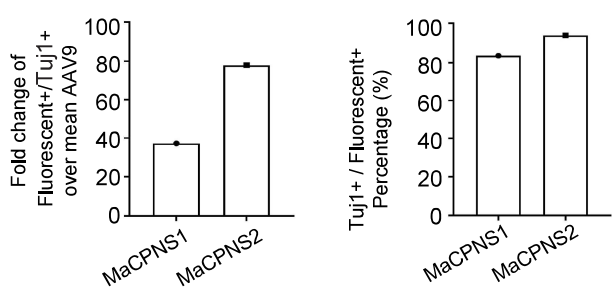
**E.**



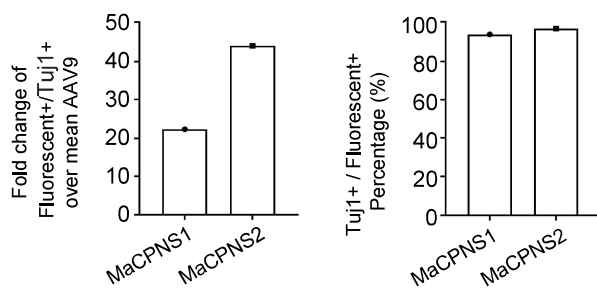
**F.**



Lumbar DRG Quantification



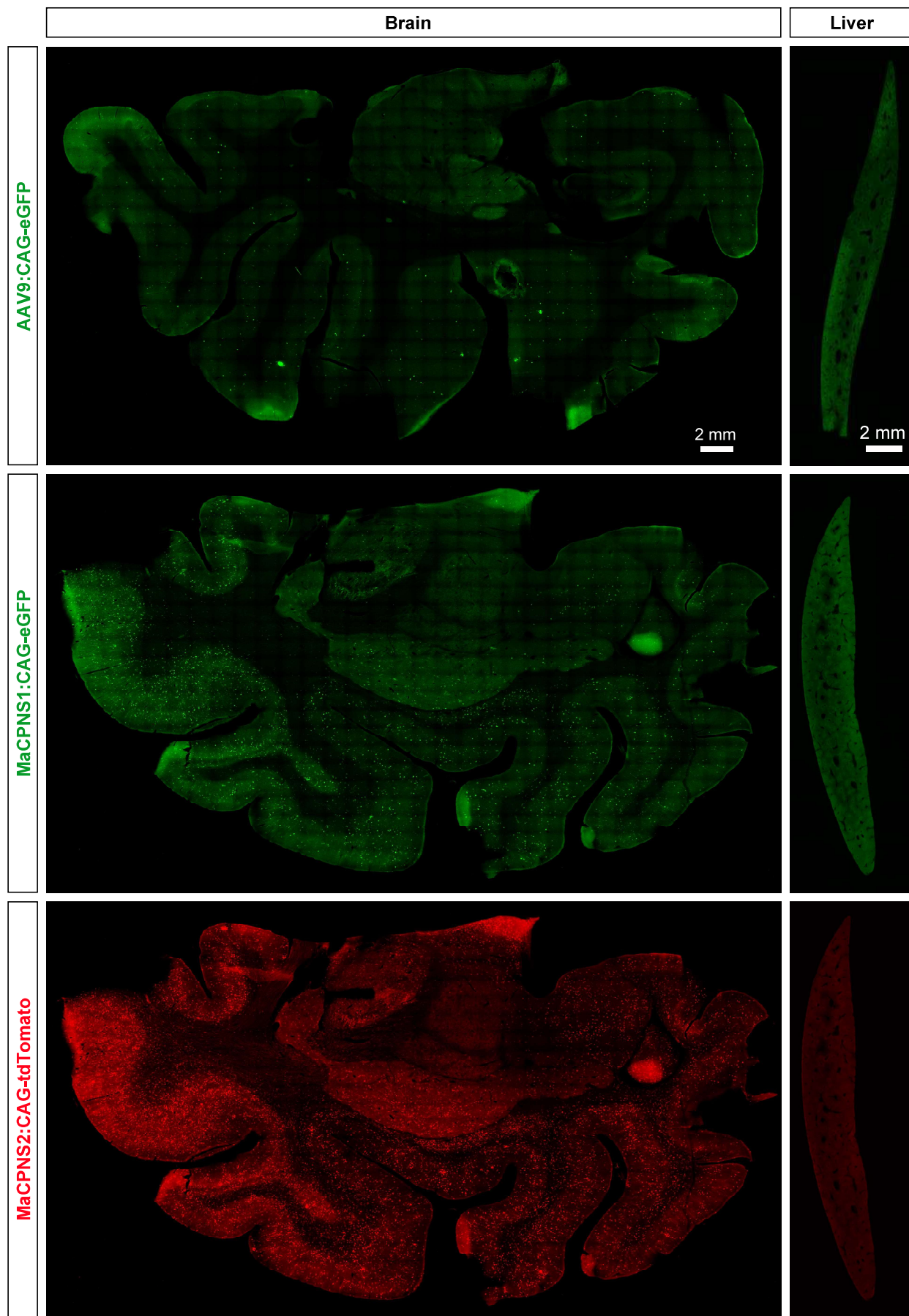
Thoracic DRG Quantification



**Supplementary Figure 5. Engineered vectors transduce spinal cord and DRG in macaque efficiently. Related to Figure 6.**

**A.** Representative images of AAV9, MaCPNS1 and MaCPNS2 vector-mediated fluorescent protein expression in the macaque lumbar spinal cord (scale bar: 500  $\mu$ m) with zoomed-in views of each channel (scale bar: 100  $\mu$ m). Slices were co-stained with NeuN (white). **B.** Quantification of the fold change of Fluorescent+/marker over mean AAV9 in lumbar spinal cord. Each data point is a slice. **C.** Representative images of MaCPNS1 and MaCPNS2 vector-mediated fluorescent protein expression in the macaque thoracic spinal cord and coccygeal spinal cord (scale bar: 500  $\mu$ m). **D.** Quantification of the fold change of Fluorescent+/marker over mean AAV9 in thoracic spinal cord. Each data point is a slice. **E, F.** (Top Panel) Representative images of AAV9, MaCPNS1 and MaCPNS2 vector-mediated fluorescent protein expression in the macaque lumbar DRG and thoracic DRG (scale bars: 50  $\mu$ m). Slices were co-stained with Tuj1 (blue). (Bottom Panel) Quantification of the fold change of Fluorescent+/marker over mean AAV9 in DRGs and percentage of Tuj1+ within the fluorescent+ population. Each data point is a slice.

Supplementary Figure 6: Novel variants efficiently transduce macaque CNS while maintaining similar transduction in liver comparing to AAV9

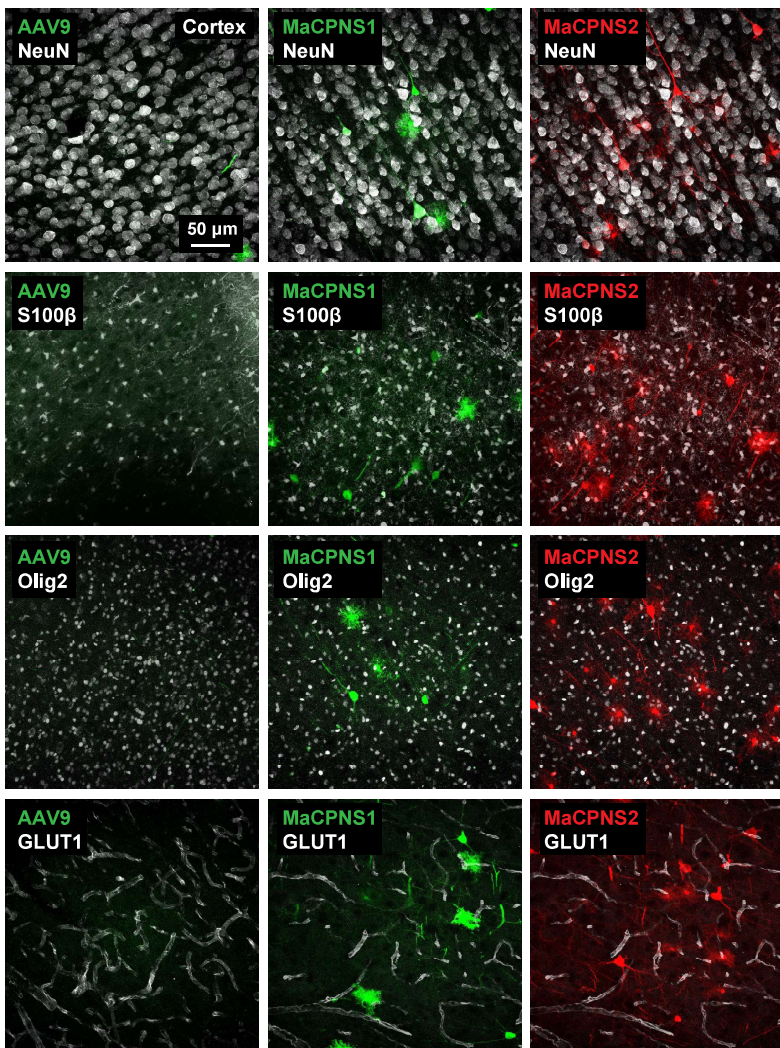


**Supplementary Figure 6. Novel variants efficiently transduce macaque CNS while maintaining similar transduction in liver compared to AAV9. Related to Figure 6.**

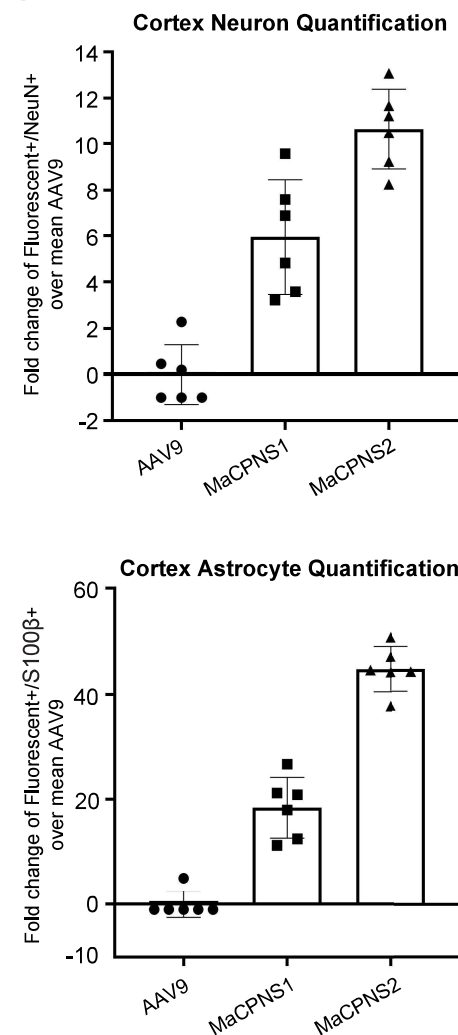
AAV capsids (AAV9/MaCPNS1/MaCPNS2) and their corresponding genomes (ssAAV:CAG-eGFP/tdTomato) were delivered to macaque to study transduction across the CNS and PNS after 3 weeks of expression. Two AAVs packaged with different fluorescent proteins were mixed and intravenously injected at a dose of  $5 \times 10^{13}$  vg/kg per macaque (*Macaca mulatta*, female, injected within 10 days of birth,  $2.5 \times 10^{13}$  vg/kg per AAV). Representative images of the brain (left) and liver (right) are shown (scale bars: 2 mm).

Supplementary Figure 7 : Cell-type profiles of engineered AAVs in macaque brain

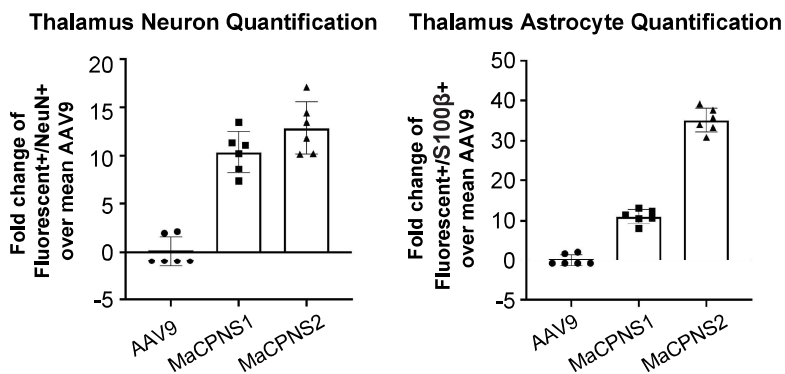
A.



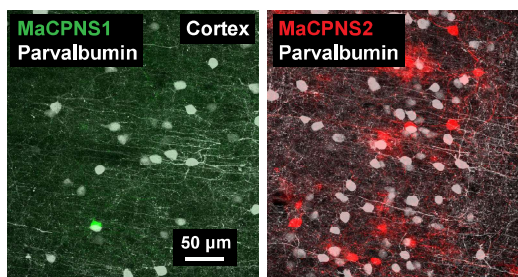
B.



C.



D.



**Supplementary Figure 7. Cell-type profiles of engineered AAVs in macaque brain.  
Related to Figure 6.**

**A.** Representative images of AAV9, MaCPNS1 and MaCPNS2 vector-mediated fluorescent protein expression in the macaque cortex and thalamus (scale bar: 50  $\mu$ m). Slices were co-stained with NeuN (first row, white), S100 $\beta$  (second row), Olig2 (third row) or GLUT1 (fourth row). **B, C.** Quantification of the fold change of Fluorescent+/marker over mean AAV9 in cortex and thalamus. Each data point is a slice. **D.** Representative images of MaCPNS1 and MaCPNS2 vector-mediated fluorescent protein expression in the macaque cortex (scale bar: 50  $\mu$ m). Slices were co-stained with Parvalbumin (white).

Table S1. Main features of novel AAVs across species following systemic delivery.

	<b>Mouse</b>	<b>Rat</b>	<b>Marmoset</b>	<b>Macaque</b>
<b>MaCPNS1</b>	<ul style="list-style-type: none"> <li>efficient transduction of sensory ganglia (NG/DRG)</li> <li>demonstrated functional readout and modulation of sensory ganglia</li> </ul>	<ul style="list-style-type: none"> <li>transduction of sensory ganglia (DRG/TG), sympathetic chain ganglia, mixed sympathetic-parasympathetic ganglia and enteric ganglia across SI and LI</li> <li>transduction of sensory nerve fibers entering SC and ascending afferent tracts in dorsal column</li> <li>observed labeling of neurons across brain</li> </ul>	<ul style="list-style-type: none"> <li>enhanced transduction of DRG, SI and ascending fiber tracts in dorsal column of the SC</li> <li>robust transduction of neurons and astrocytes</li> <li>more biased to neurons in the brain</li> </ul>	<ul style="list-style-type: none"> <li>enhanced transduction of DRG</li> <li>transduction of sensory nerve fibers entering SC and ascending afferent tracts in dorsal column</li> <li>robust transduction of neurons and non-neuronal cells in brain and SC</li> <li>more biased to neurons</li> </ul>
<b>MaCPNS2</b>	<ul style="list-style-type: none"> <li>efficient transduction of sensory ganglia (NG/DRG)</li> <li>efficient transduction of ENS, especially SI</li> </ul>	<ul style="list-style-type: none"> <li>transduction of sensory ganglia (DRG/TG), sympathetic chain ganglia, mixed sympathetic-parasympathetic ganglia and enteric ganglia across SI and LI</li> <li>transduction of sensory nerve fibers entering SC and ascending afferent tracts in dorsal column</li> <li>observed labeling of neurons across brain</li> </ul>	<ul style="list-style-type: none"> <li>enhanced transduction of DRG, SI and ascending fiber tracts in dorsal column of the SC</li> <li>robust transduction of neurons and astrocytes in the brain</li> </ul>	<ul style="list-style-type: none"> <li>enhanced transduction of DRG and GI tract, including esophagus, colon and SI</li> <li>transduction of sensory nerve fibers entering SC and ascending afferent tracts in dorsal column</li> <li>robust transduction of neurons and non-neuronal cells in brain and SC</li> </ul>

NG: nodose ganglia; DRG: dorsal root ganglia; SI: small intestine; LI: large intestine; SC: spinal cord.

**Table S1. Main features of novel AAVs across species following systemic delivery, related to Figure 6.**